Heliyon 7 (2021) e07634

Contents lists available at ScienceDirect

Heliyon

journal homepage: www.cell.com/heliyon

Research article

Quantum chemical calculation, performance of selective antimicrobial activity using molecular docking analysis, RDG and experimental (FT-IR, FT-Raman) investigation of 4-[{2-[3-(4-chlorophenyl)-5-(4-propan-2-yl) phenyl)-4, 5-dihydro- 1H- pyrazol-1-yl]-4-oxo-1, 3- thiazol-5(4H)-ylidene} methyl] benzonitrile

N. Shanmugapriya [a], V. Balachandran [a,*], B. Revathi [a], B. Narayana [b], Vinutha V. Salian [b], K. Vanasundari [a], C. Sivakumar [a]

[a] Centre for Research, Department of Physics, Arignar Anna Government Arts College (Affiliated to Bharathidasan University), Tiruchirappalli, Musiri, 621 211, India
[b] Department of Studies in Chemistry, Mangalore University, Mangalagangotri, 574 199, India

ARTICLE INFO

Keywords:
Thiazole
DFT
RDG
ELF
Docking
Antimicrobial activity

ABSTRACT

The research received a great deal of worldwide attention due to the nature of interpretation before the experimental process. Based on the systematic process the structure of thiazole -pyrazole compound 4-[{2-[3-(4-chlorophenyl)-5-(4-propan-2-yl) phenyl)-4, 5-dihydro- 1H- pyrazol-1-yl]-4-oxo-1, 3- thiazol-5(4H)-ylidene} methyl] benzonitrile [CPTBN] was investigated. In the first level, the spectral statistics on experimental FT-IR and FT-Raman was reported. At the next level, geometrical parameters was theoretically acquired from density functional theory (DFT) using B3LPY/6-31G and 6-311G basis set. The computed Wavenumber were collected and compared with the experimental data. The vibrational modes were interpreted in terms of potential energy distribution (PED) results. The FMO, MEP, and NBO analysis further validated the electrophilic and nucleophilic interaction in the molecular systems. Two grams-positive bacteria: *staphylococcus aureus, Bacillus subtilis* and two gram-negative bacteria: *Esherichia coli, Pseudomonas aeruginosa* was performed for antibacterial activity. Two fungal strain *Candida albicans* and *Aspergillus Niger* was carried out against a ligand using anti-fungal activity. The molecular docking analysis explores the antimicrobial and selective potential inhibitory nature of the binding molecule. Besides, RDG and ELF analysis were also performed to show the nature of interactions between the molecule.

1. Introduction

Recently, the investigation of vibrations of substituent azoles compounds was an incredible arrangement of enthusiasm among the spectroscopists because of their physical and chemical properties. Thiazole is one of the most intensively studied classes of aromatic amalgamation that was initially outlined by Hantzsch and Weber in 1887 [1]. It belongs to the family of azoles, the heterocyclic five-membered compounds containing sulphur and nitrogen atoms at 1,3 positions in their fragrant ring structure [2]. Thiazole core occupies a very important position among the heterocyclic compounds which is naturally bioactive. Attached to various active elements like pyrazole, phenyl, nitrile contains compounds were synthesized in a laboratory environment and were eventually introduced to be used to treat various diseases and varieties of industrial purposes such as fungicides, dye, and paint production [3, 4]. Consistently, the active elements nitrile are a common choice as both a chemical and physical barrier to these hazards, especially nitrile gloves were useful to a huge number of human services and industry laborers who are exposed to chemical and organic risks [5]. Benzonitrile often plays a key role in the inhibition of hydrogen absorption [6]. The present work involves the study of comprehensive molecular geometry and vibrational modes of CPTBN using quantum chemical computations. It has a molecular formula $C_{29}H_{23}ClN_4OS$. The global reactivity descriptors like highest occupied molecular orbital (HOMO), lowest unoccupied molecular orbital (LUMO), and molecular electrostatic potential (MEP) analysis were interpreted with the theoretical value. The energy gap values (ΔE)

* Corresponding author.
E-mail address: brsbala@rediffimail.com (V. Balachandran).

https://doi.org/10.1016/j.heliyon.2021.e07634
Received 28 November 2020; Received in revised form 27 December 2020; Accepted 19 July 2021

have been calculated using B3LYP/6-31G and 6-311G basis sets and reported as a result of the molecular transitions. The investigation of natural bond orbital (NBO) provides information on the chemical features such as intra and intermolecular charge transfer, second-order perturbation characteristic relationships between the Lewis (donor) and non-Lewis (acceptor) [6, 7]. The title molecule's reduced density gradient (RDG) and electron localization function (ELF) were investigated using Multiwfn software. The disc diffusion method was used to successfully evaluate anti-microbial activity of the compound at 25, 50, 75, and 100 μg/ml concentration levels with established bacterial and fungus strains. To explore the potential biological activity of the thiazole (CPTBN) compound, few studies included in the molecular docking analysis and report on the drug-like behaviors of the title compound. The anti-microbial, monoclonal antibodies, Nitric oxide synthase inhibitor, and Staphylococcal protein A protein structural activity observed were consistent with the results of docking pose providing key insight of selective antimicrobial and medical potential inhibitors. The above findings are opening up new avenues of medicinal chemistry and important for clinical manifestation.

2. Experimental details

The structure of CPTBN along with the synthesis procedure was screened by Salian et al. [8] intrinsically and were used for spectral measurements. For the compound characterization,

- Fourier transform infrared spectrum was recorded between 4000-0 cm^{-1} using a Perkin Elmer spectrometer, which was calibrated using an MCT Mid-IR range detector with KBr (potassium bromide) pellets technique.
- FT-Raman spectrum were obtained within the interval of 3500-0 cm^{-1} using a Bruker RFS27 the 1064 nm line of a Nd: YAG laser device for excitation controlled at 200 mW power. At room temperature, the spectrum was recorded at a scanning speed of 10 cm^{-1} and a spectral resolution of 1.0 cm^{-1}.
- Using the disc diffusion method, the title compound with four concentrations of 25, 50, 75, and 100 μg/ml in distilled DMSO was prepared and tested against antimicrobial strains were maintained on agar medium at 4 °C. Antimicrobial cultures such as *Staphylococcus aureus, Bacillus subtilis, Esherichia coli, Pseudomonas aeruginosa, Candida albicans* and *Aspergillus Nige* were tested.

3. Computational details

In the present work, geometry optimizations and electronic structure calculation of the CPTBN were first performed for B3LYP functional with 6-31G and 6-311G basis sets using the Gaussian 09 program [9]. The correlation function is used to predict the molecular structure of the CPTBN. The potential energy distribution (PEDs) is done with the help of (VEDA) program [10]. GAUSSVIEW program [11] provided a visual presentation of vibrational modes.

Screening the calculations exposed that, the density functional theory (DFT) computations with the promising vibrational properties, molecular geometry, and orbital energy of CPTBN. Besides natural bond orbital (NBO) calculations were carried out using the NBO program implemented in Gaussian 09 [12]. Multi-wfn software provides a route for a consistent description of interactions between the atoms in terms of the topological properties of the electron density ρ(r). Electron localization function (ELF) map and Reduced Density Gradient (RDG) were calculated using the Multi-wfn program [13]. Molecular docking studies were performed with the help of an Auto dock [14] software. Discovery Studio Visualizer 4.1 [15] and Pymol software [16].

4. Results and discussions

4.1. Molecular geometry

The density functional theory is one of the most reliable computational approaches for the theoretical investigation of the structure of the molecule. The Gaussian 09 shows an optimized molecular form of CPTBN computed by B3LYP/6-31G, B3LYP/6-311G, and visualized through the Gauss view program shown in Figure 1. The optimized bond lengths and angles of the title compound are tabulated in Tables 1 and 2, respectively. The optimized structure is found to be with C1 point group symmetry having its ground state energy of 2271.46 a.u with a dipole moment of 8.9529 Debye. Elaboration of the collected data is as follows.

The optimized geometrical structure of the title molecule benzonitrile substituent in the thiazole ring system, chain with pyrazol bounds by two phenyl rings (one is chlorophenyl - PhI and the other is 4-(Propan-2-yl) phenyl - PhII. Normally, the C–C bond lengths of aromatic rings formed by the phenyl ring are greater than range 1.3900 Å, although the computed value falls in the range C_4–C_6 = 1.4102/1.4120 Å, C_9–C_{11} = 1.3933/1.3964 Å, C_5–C_7 = 1.3959/1.3977Å. for PhI and C_{14}–C_{15} = 1.4038/1.405Å, C_{16}–C_{19} = 1.3964/1.3982Å, C_{17}–C_{21} = 1.4056/1.4076 Å for PhII. The title compound is somewhat regular and the spread of C–C bond distance is 1.3900–1.5500 Å in (phenyl ring I) PhI and 1.3900–1.4500 Å in (phenyl ring II) PhII, which is similar to the report by Parveen et al. [17]. The computed bond lengths of the C=C double bond values are C_4–C_5 = 1.4067/1.4083Å, C_6–C_9 = 1.3907/1.3931Å, C_7–C_{11} = 1.3886/1.3922Å for PhI and C_{14}–C_{16} = 1.3981/1.4009Å, C_{15}–C_{17} = 1.3934/1.3957Å, C_{19}–C_{21} = 1.4011/1.4036Å for PhII. This observation reveals that the C–C atoms in both rings are between the conventional C–C single and C=C double bond lengths, indicating that the electron density is conjugated on all rings. The outer shell carbon-hydrogen bond length values are experimentally falling in the range of 0.90 Å to 1.09 Å, whereas the calculated C–H (ring) and C–H (methyl) values are 1.0800 Å and 1.0900 Å, respectively. The C–H length in both phenyl rings is found almost equal to around 1.08 Å, is very close to the experimental value 1.09 Å, which indicates that C–H bond lengths remain unaffected by the substitution in rings. Generally, the thiazole ring has a difference in bond length is due to the presence of a sulphur and nitrogen atom. The theoretical value of the C_{39}–S_{41} bond length is 1.8653/1.8592Å and the experimental value is found to be 1.86 Å [3]. The C_{40} = O_{44} carbonyl moiety present in thiazole has a double bond character, as evidenced by the compound's estimated bond length (DFT) of 1.2450/1.2472 Å. The shortening of these C–N bonds reveals the effect of resonance in this part of the molecule. It attempts to draw the electron density of the neighbouring atoms which as a result move closer together to share the electrons more easily. The literature value of C–N, C=N, C≡N bond length (XRD) is 1.3000 Å, 1.31 Å and 1.1600 Å [17]. In the current studies C_1–N_{24} = 1.3046/1.3061Å, C_2–N_{25} = 1.5079/1.5097Å present in pyrazole ring, C_{42} = N_{43} = 1.3051/1.3059Å present in thiazole ring, and C_{57} ≡ N_{58} = 1.1682/1.1748Å present in benzonitrile ring indicating that π-electron in the molecules are delocalized in the C–C of the molecule which is similar in reported by Mustafa Er et al. [18]. The chlorine is extremely electronegative, it strives to get more electron density, and the computed value is 1.825 Å, that is found near the phenyl ring PhI. The experimental values are taken from similar C–Cl bond length is observed in 1.8200 Å by Vanasundari et al. [19]. The magnitude of the length N–N bond is described in 1.38 Å assigned by Priyanka Singh et al. [20] and is found in the center to be 1.3963/1.3946Å for the CPTBN molecule. The angle formed between two adjacent bonds shows the internal bond angles N_{25}–C_{42}–N_{43}, C_1–N_{24}–N_{25}, C_{39}–C_{40}–O_{44} and N_{43}–C_{40}–O_{44} are found around the range to be 123°, 108°, 124°, and 122° in the CPTBN respectively. This shortest bond angle is formed between thiazol is C_{39}–S_{41}–C_{42} in 86°.

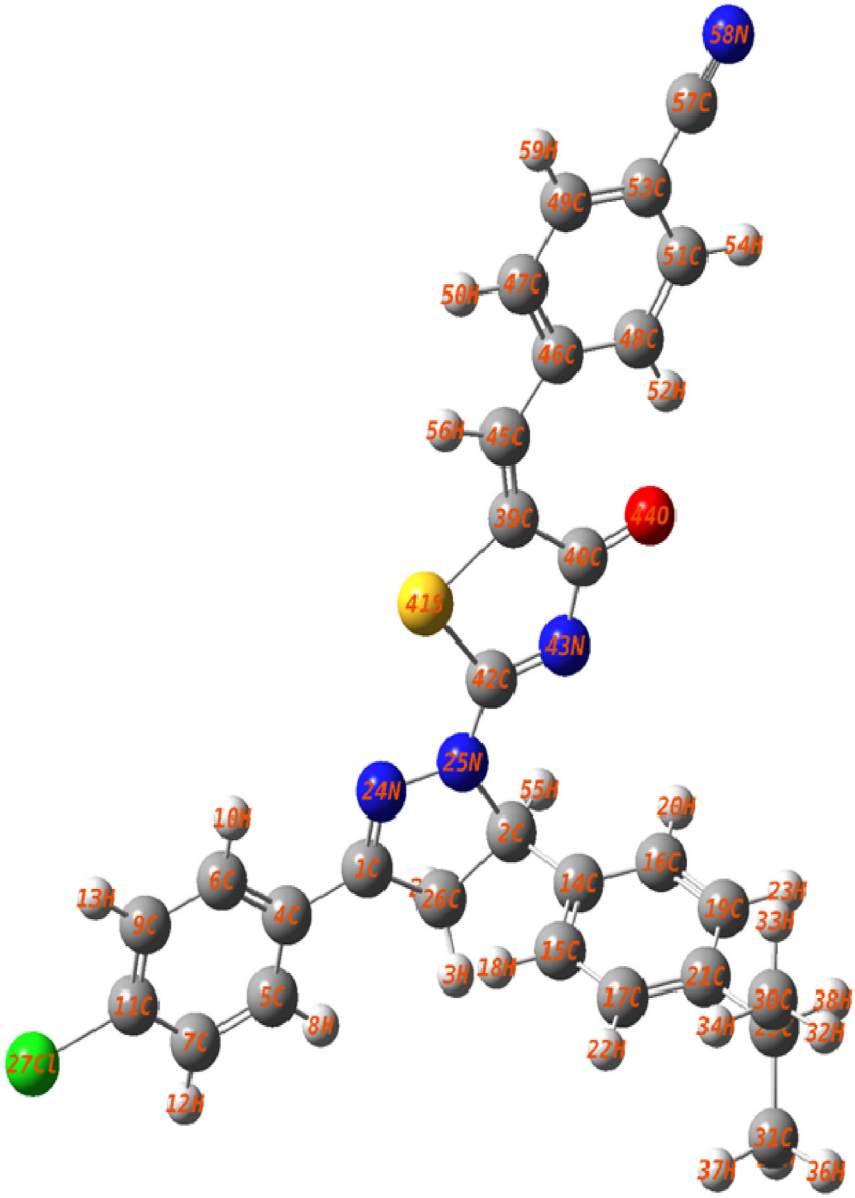

Figure 1. Optimized structure of CPTBN using B3LYP/6-311G basis set.

4.2. Vibrational assignments

The main aim of this vibrational calculation is to provide a clear interpretation of both experimental and theoretical results. The experimental calculation was carried out using IR and Raman (Figures 2 and 3). Comparative theoretical calculations were performed using the B3LYP method with 6–31 G and 6-311G basis sets were reported in Table 3. Generally, the vibrational modes of a compound with N atoms are more complex, with 3N 5 vibrational modes for a linear compound and 3N 6 modes for a nonlinear compound. On specifying three rotational and one translational degrees of freedom (3N-6) of CPTBN under (C1) point group symmetry has 59 atoms and 171 fundamental vibrational modes. Based on the optimized structure, the detailed spectral information is interpreted as follows.

4.2.1. C– H vibrations

The spectrum of a compound represents its energy absorption pattern is represented by the regions. In the present study, there are three different benzene rings attached to the combination of thiazole with pyrazol. The occurrence of benzene C–H stretching vibration extends often above 3000 cm^{-1} for aromatic composition and less than 3000 cm^{-1} for non-aromatic composition. In the FT-IR, FT-Raman spectra, aromatic compounds predominantly have a C–H vibration of 3000–3100 cm^{-1}. The essence and location of the replacement are affected in this region by the band. Because of their high polarization, these C–H detention modes typically appear with Raman strength. A spectrum of FT-Raman, its aromatic stretching mode C–H was used for the observation of the observed band 3074 cm^{-1} and 3053 cm^{-1} by Sathish et al. [21]. In the case of the title compound, it exhibits multiple weak band's shoulders on the stronger C– H stretching vibration in the region 3067 cm^{-1}, 3013 cm^{-1}, 2957 cm^{-1} and 2868 cm^{-1} vibrational magnitude by B3LYP/6-311G. Normally, the C–H in-plane vibrational bending mode occurs in the region 1530- 1000 cm^{-1}. Spectrum of C–H in-plane vibrational bending mode observed at 1424 cm^{-1} (w), 1396 cm^{-1} (ms), and 1114 cm^{-1} (ms) in FT-IR spectrum and 1285 cm^{-1} (ms), 1251 cm^{-1} (s), 1173 cm^{-1} (ms) in FT-Raman spectrum, the computed wavenumbers for this mode were coincident with 1429, 1394, 1290, 1251, 1120 cm^{-1} for B3LYP/6-31G and 1425, 1395, 1286, 1250, 1116 cm^{-1} for B3LYP/6-311G. The out-of-plane C–H bending mode of the phenyl ring are observed at 804 cm^{-1}(IR), 928, 832, 806 cm^{-1} (FT-Raman) and

Table 1. Optimized structural parameters (bond length) of CPTBN calculated by DFT/B3LYP method with 6-31G and 6-311G basis sets.

S.No	Bond Length (Å)	B3LYP/6-31G	B3LYP/6-311G	S.No	Bond Length (Å)	B3LYP/6-31G	B3LYP/6-311G
1	C1–C4	1.4607	1.4604	33	C26–H28	1.0923	1.0968
2	C1–N24	1.3046	1.3061	34	C29–C30	1.5450	1.5465
3	C1–C26	1.5198	1.5219	35	C29–C3I	1.5446	1.5461
4	C2–C14	1.5176	1.5182	36	C29–H38	1.0949	1.0993
5	C2–N25	1.5079	1.5097	37	C30–H32	1.0923	1.0965
6	C2–C26	1.5552	1.5570	38	C30–H33	1.0910	1.0953
7	C2–H55	1.0875	1.0918	39	C30–H34	1.0925	1.0968
8	H3–C26	1.089	1.0934	40	C31–H35	1.0913	1.0956
9	C4–C5	1.4067	1.4083	41	C31–H36	1.0922	1.0964
10	C4–C6	1.4102	1.4120	42	C31–H37	1.0925	1.0968
11	C5–C7	1.3959	1.3977	43	C39–C40	1.5001	1.5028
12	C5–H8	1.0810	1.0844	44	C39–S41	1.8653	1.8592
13	C6–C9	1.3907	1.3931	45	C39–C45	1.3535	1.3576
14	C6–H10	1.0799	1.0835	46	C40–N43	1.4008	1.4006
15	C7–C11	1.3886	1.3922	47	C40–O44	1.2450	1.2472
16	C7–H12	1.0792	1.0828	48	S41–C42	1.8449	1.8442
17	C9–C11	1.3933	1.3964	49	C42–N43	1.3051	1.3059
18	C9–H13	1.0793	1.0829	50	C45–C46	1.4644	1.4649
19	C11-CL27	1.8250	1.8222	51	C45–H56	1.0864	1.0896
20	C14–C15	1.4038	1.4059	52	C46–C47	1.4165	1.4184
21	C14–C16	1.3981	1.4009	53	C46–C48	1.4123	1.4146
22	C15–C17	1.3934	1.3957	54	C47–C49	1.3868	1.389
23	C15–H18	1.0832	1.0866	55	C47–H50	1.0824	1.0858
24	C16–C19	1.3964	1.3982	56	C48–C51	1.3905	1.3927
25	C16–H20	1.0814	1.0850	57	C48–H52	1.0776	1.0815
26	C17–C21	1.4056	1.4076	58	C49–C53	1.4073	1.4098
27	C17–H22	1.0823	1.0858	59	C49–H59	1.0806	1.084
28	C19–C21	1.4011	1.4036	60	C51–C53	1.4067	1.4092
29	C19–H23	1.0827	1.0861	61	C51–H54	1.0807	1.0842
30	C21–C29	1.5251	1.5260	62	C53–C57	1.4301	1.4303
31	N24–N25	1.3963	1.3946	63	C57–N58	1.1682	1.1748
32	N25–C42	1.3427	1.3433				

Ref [17, 18, 19, 20].

computed values in the range 932- 810 cm^{-1} (DFT) by Begum et al. [22]. The correlated scale vibrations observed at wavenumbers 896 (w), 829 (ms), 811 cm^{-1} (w) (FT-IR) and 945 cm^{-1} (m) (FT-Raman) are coincident with 933, 900, 833, 814 cm^{-1} for B3LYP/6-31G and 932, 898, 829, 810 cm^{-1} for B3LYP/6-311G.

4.2.2. Methyl group vibrations

For the assignments of benzene ring has a methyl CH_3 group was expected in nine fundamental modes, namely symmetrical stretch, asymmetrical stretch, symmetric deformations, asymmetrical deformations, in-plane (δ), out-of-plane (γ), in-plane rocking (δ_{rock}), out-of-plane rocking (γ_{rock}), and twisting bending (Γ CH_3) [23]. From the structure of the title molecule possesses two CH_3 (5-(4-Propan-2-yl) phenyl)) group substitutions in the pyrazole ring chain. The symmetric and asymmetric methyl group stretching band can be observed in the region 2942-2879 cm^{-1}.

Naturally, the CH_3 group related to electron-donating substitutions that bind to the same ring systems. These vibrations attain amplitude of 3000-2840 cm^{-1}. The CH_3 asymmetric stretching vibration is recorded in the FT-IRs spectrum at 2929 (w) cm^{-1} FT-Raman spectrum at 2947 (w) cm^{-1}, 2933 (w) cm^{-1}. Theoretically computed mode having wavenumber at 2952, 2936, 2934 cm^{-1} for B3LYP/6-31G and 2948, 2932, 2930 cm^{-1} for B3LYP/6-311G. The aromatic ring has a weak symmetric stretching vibration value that appears in the region 2903, 2881 cm^{-1} for B3LYP/6-31G and 2900, 2879 cm^{-1} for B3LYP/6-311G. The in-plane vibrations (δ_{ipb}) bending mode has been calculated at 1390, 1385, 998 cm^{-1} (6-31G), and 1389, 1382, 998 cm^{-1} (6-311G). The out-of-plane bending vibrations of title compound occur in medium peak (γ_{opb}) 1409 (ms) cm^{-1} FT-Raman is assigned and deformation is predicted at a range (γ_{opb}) 1420, 1415, 1025 cm^{-1} for B3LYP/6-31G and 1418, 1410, 1021 cm^{-1} for B3LYP/6-311G. The rocking mode of the CH_3 group is computed at 1103, 1025 cm^{-1} for B3LYP/6-31G and 1100, 1021 cm^{-1} for B3LYP/6-311G well in agreement with a recorded value of 1099 cm^{-1} in the FT-Raman spectrum. Moreover, the twisting vibration of ΓCH_3 falls below 500 cm^{-1}. In the present study twisting CH_3 deformations vibrations possessed at 181 (w) in FT-Raman spectrum, at 185 cm^{-1} B3LYP/6-31G and 180cm^{-1} in B3LYP/6-311G in with the PED contribution is 58 %.

4.2.3. CH_2 vibrations

Methylene (CH_2) vibration is formed due to the presence of pyrazole in the title molecule which creates four fundamental frequencies out of six and follows an anti-symmetric stretching mode-ν_{ass} (CH_2), asymmetric stretching mode-ν(CH_2), a scissoring mode-sis (CH_2), twisting mode- Γ (CH_2) and a rocking mode-ρ(CH_2). According to the literature, CH_2 symmetric and asymmetric vibration fall in the range around 3000-2800 cm^{-1} [24]. The CH_2 asymmetric stretching modes are computed at 2955, 2915 cm^{-1} for B3LYP/6-31G and 2953, 2912 cm^{-1} for B3LYP/6-311G, but no peak can be seen in this region on a recorded spectrum. The bending mode, which involves a hydrogen atom attached to the core carbon, is between 1450 and 875 cm^{-1}, although there is a coupling of vibration modes that generally occurs, especially CH_2 scissoring and rocking, which are more sensitive to the molecular

Table 2. Optimized structural parameters (bond angle) of CPTBN calculated by DFT/B3LYP method with 6- 31Gand6-311G basis sets.

S.No	Bond angle (degree)	B3LYP/6-31G	B3LYP/6-311G	S.No	Bond angle (degree)	B3LYP/6-31G	B3LYP/6-311G
1	C4–C1–N24	121.66	121.57	54	C2–C26–H28	111.73	111.63
2	C4–C1–C26	125.16	125.26	55	H3–C26–H28	107.50	107.49
3	N24–C1–C26	113.17	113.16	56	C21–C29–C30	111.67	111.74
4	C14–C2–N25	112.28	112.16	57	C21–C29–C31	111.97	112.07
5	C14–C2–C26	115.28	115.36	58	C21–C29–H38	107.05	106.93
6	C14–C2–H55	109.32	109.24	59	C30–C29–C31	110.93	111.07
7	N25–C2–C26	100.08	100.12	60	C30–C29–H38	107.46	107.36
8	N25–C2–H55	107.21	107.31	61	C31–C29–H38	107.48	107.37
9	C26–C2–H55	112.16	112.15	62	C29–C30–H32	110.48	110.46
10	C1–C4–C5	120.62	120.65	63	C29–C30–H33	111.13	111.11
11	C1–C4–C6	120.57	120.67	64	C29–C30–H34	111.11	111.21
12	C5–C4–C6	118.81	118.69	65	H32–C30–H33	108.29	108.22
13	C4–C5–C7	120.86	120.92	66	H32–C30–H34	107.81	107.81
14	C4–C5–H8	120.29	120.37	67	H33–C30–H34	107.90	107.91
15	C7–C5–H8	118.86	118.71	68	C29–C31–H35	111.19	111.16
16	C4–C6–C9	120.73	120.78	69	C29–C31–H36	110.45	110.43
17	C4–C6–H10	119.09	119.12	70	C29–C31–H37	111.19	111.29
18	C9–C6–H10	120.18	120.10	71	H35–C31–H36	108.24	108.17
19	C5–C7–C11	118.80	118.74	72	H35–C31–H37	107.92	107.94
20	C5–C7–H12	120.73	120.72	73	H36–C31–H37	107.72	107.72
21	C11–C7–H12	120.47	120.53	74	C40–C39–S41	108.92	108.90
22	C6–C9–C11	118.96	118.93	75	C40–C39–C45	132.84	132.96
23	C6–C9–H13	120.71	120.71	76	S41–C39–C45	118.24	118.14
24	C11–C9–H13	120.32	120.36	77	C39–C40–N43	113.46	113.45
25	C7–C11–C9	121.84	121.95	78	C39–C40–O44	124.41	124.31
26	C7–C11-CL27	119.10	119.07	79	N43–C40–O44	122.14	122.24
27	C9–C11-CL27	119.06	118.99	80	C39–S41–C42	86.38	86.28
28	C2–C14–C15	121.47	121.46	81	N25–C42–S41	119.48	119.70
29	C2–C14–C16	119.90	120.00	82	N25–C42–N43	123.19	123.01
30	C15–C14–C16	118.63	118.54	83	S41–C42–N43	117.33	117.29
31	C14–C15–C17	120.62	120.67	84	C40–N43–C42	113.91	114.08
32	C14–C15–H18	120.23	120.30	85	C39–C45–C46	134.89	134.95
33	C17–C15–H18	119.15	119.03	86	C39–C45–H56	113.98	113.95
34	C14–C16–C19	120.53	120.59	87	C46–C45–H56	111.13	111.10
35	C14–C16–H20	119.55	119.56	88	C45–C46–C47	115.75	115.85
36	C19–C16–H20	119.90	119.82	89	C45–C46–C48	126.30	126.28
37	C15–C17–C21	121.06	121.10	90	C47–C46–C48	117.96	117.87
38	C15–C17–H22	119.11	119.04	91	C46–C47–C49	121.69	121.70
39	C21–C17–H22	119.84	119.86	92	C46–C47–H50	119.20	119.23
40	C16–C19–C21	121.24	121.28	93	C49–C47–H50	119.11	119.07
41	C16-19-H23	119.38	119.35	94	C46–C48–C51	120.52	120.58
42	C21–C19–H23	119.37	119.37	95	C46–C48–H52	119.11	119.14
43	C17–C21–C19	117.91	117.82	96	C51–C48–H52	120.37	120.29
44	C17–C21–C29	121.37	121.41	97	C47–C49–C53	119.75	119.80
45	C19–C21–C29	120.71	120.76	98	C47–C49–H59	120.49	120.42
46	C1–N24–N25	108.58	108.59	99	C53–C49–H59	119.77	119.78
47	C2–N25–N24	113.47	113.35	100	C48–C51–C53	120.85	120.87
48	C2–N25–C42	125.02	124.98	101	C48–C51–H54	119.73	119.66
49	N24–N25–C42	121.46	121.62	102	C53–C51–H54	119.43	119.47
50	C1–C26–C2	103.65	103.71	103	C49–C53–C51	119.24	119.17
51	C1–C26–H3	112.34	112.39	104	C49–C53–C57	120.26	120.29
52	C1–C26–H28	110.44	110.44	105	C51–C53–C57	120.50	120.54
53	C2–C26–H3	111.23	111.25				

environment. The twisting mode of the CH_2 group is computed at 1196 cm^{-1} (6-31G) and 1194 cm^{-1} (6-311G) agree with the recoded value of 1195 cm^{-1} FT-IR and 1196 cm^{-1} FT-Raman. The mode scissoring value 1375 cm^{-1}(w) in FT-Raman spectrum compared with computed wave-number 1379 cm^{-1} for B3LYP/6-31G and 1376 cm^{-1} for B3LYP/6-311G.

4.2.4. Nitrile vibrations

Nitrogen compounds with cumulated double bonds or triple bonds, such as nitrile and cyanates, have a specific spectrum, typically with a single, usually intense absorption peak at 2280–2200 cm^{-1} [6,25]. The saturated cyclic nitrile is detected by the presence of a band near 2250 cm^{-1} while their aromatic counterparts absorb at lower frequencies near

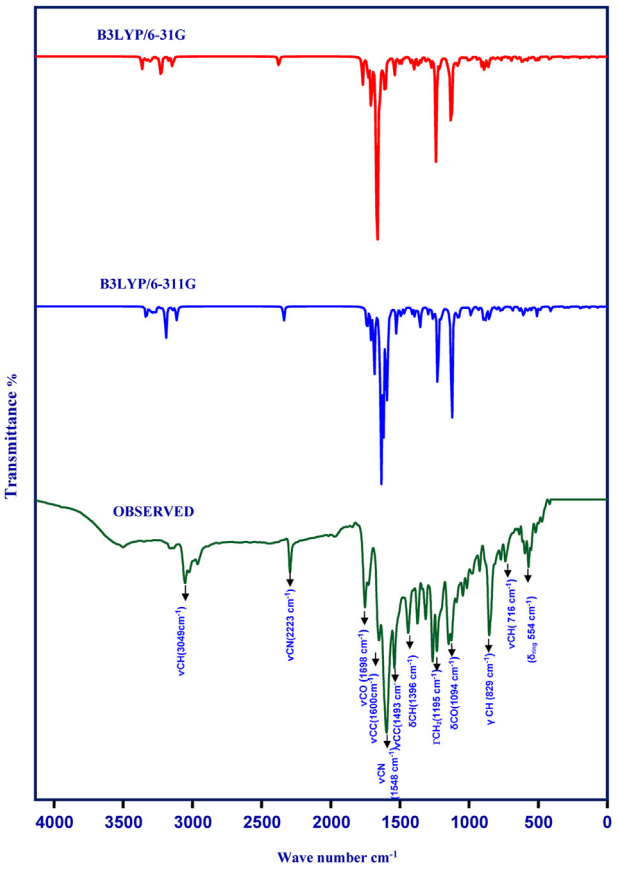

Figure 2. Observed FT-IR and simulated spectra of CPTBN.

2230 cm^{-1}. Generally, the IR and Raman spectrum exhibits C≡ N is stretching vibrations at 2235 cm^{-1} and 2290 cm^{-1}. Similarly, the large range that has been reported against or appearance of C≡ N is 2223 (w) cm^{-1} for FT-IR and 2222 (m) cm^{-1} for FT-Raman, but also supported by the appearance of medium-strong stretching bands. Around 1738 cm^{-1} and 1698 cm^{-1} for a cyclic ring in the compounds, that confirm the formation of [3 + 2] ring condensation product reported by Bardak et al. [26] The correlated scale vibrations of PED contribution observed in 1300, 1550 cm^{-1} at 6-31G, 1296,1548 cm^{-1} at 6-311G and experimental at 1548 cm^{-1} (vs) cm^{-1} in FT-IR spectrum.

4.2.5. C–C vibrations

In general, the stretching vibration of heterocyclic aromatic compounds C–C bond occurs in the region 1650-1200 cm^{-1} reported by Sheeja Mol et al. [27]. In the present study, a medium-strong band is observed in 1493 (ms) cm^{-1} at FT-IR spectrum and 1441(w), 1551(m) cm^{-1} at FT-Raman spectrum, the strong band is observed in the corresponding computed DFT value is 1442, 1552 cm^{-1} for 6-31G and 1440, 1550 cm^{-1} for 6-311G. The title molecule has five rings with C–C stretching vibrations and form peaks arising in the array at 1631-1025 cm^{-1} [28]. A combination of C–H vibration present in stretching C–C bond locate the very strong frequency in 1600 cm^{-1} near FT-IR and 1594, 1561 cm^{-1} near FT-Raman. The predicted corresponding value lie at 1600, 1564 cm^{-1} in 6-31G and 1598, 1562 cm^{-1} in 6-311G. The combination of stretching C–C and in-plane C–C vibration locate the very strong frequency in both FT-IR and FT-Raman is 1225 cm^{-1}. The ring carbon-carbon stretching vibration occur in the region 1625-1400 cm^{-1} routed by Fatma et al. [25] is compared with the values. The C–C stretching at 1428 cm^{-1}, 1235 cm^{-1}, 1002 cm^{-1} in the IR spectrum and 1579 cm^{-1}, 1531 cm^{-1}, 1439 cm^{-1}, 1380 cm^{-1}, 1123 cm^{-1} in the Raman spectrum are assigned by Kuruvilla et al. [29]. In the present case, bending and ring vibration of C–C falls below 1000 cm^{-1} and are shown in Table 3. The C–C in-plane bending medium band occurs between 1000-600 cm^{-1} [28]. A medium intense FT-Raman band is identified at 823 cm^{-1}, which corresponds to the calculated value lies at 826 cm^{-1} in 6-31G and 821 cm^{-1} in 6-311G. From the FT-Raman spectrum the values predicted at δ_{ring} = 945ms, 631m, 551vw, 353ms cm^{-1} that confirms the formation of δring in the range 632, 671, 622, 339, 332, 327, 310, 81, 76, 71, 23 cm^{-1} for B3LYP/6-311G and δring in the range 684, 675, 625, 340, 334, 331, 314, 84, 75, 25 23 cm^{-1} for B3LYP/6-31G. The C–C in-plane bending vibration mode calculated at δ_{ipb} 695, 440, 390, 345 cm^{-1} for B3LYP/6-31G, and δ_{ipb} 694, 396, 388, 343 cm^{-1} for B3LYP/6-311G. The out-of-plane C–C bending modes of γ_{opb} in the range 850, 844, 622, 405, 375, 310, 298, 35, 29, 23, 18, 14, 8 cm^{-1} for B3LYP/6-311G and γ_{opb} in the range 855, 847, 625, 444, 379, 314, 300, 38, 30, 20, 15, 10 cm^{-1} for B3LYP/6-31G.

4.2.6. C=O vibrations

The C=O stretching of the carbonyl group is identical large dipole moment and intense stretching vibration whose peak is, generally expected in the region 1740-1660 cm^{-1}. In the present study, a moderate band was observed within the FT-IR spectrum at 1698 (ms) cm^{-1} is assignable. The C=O stretching vibrations deviate from the B3LYP/6-311G predicted value by 1659cm^{-1}. The strong band in the FT-IR and FT-Raman, near 1750- 1655 cm^{-1} confirm the possibility of a carbonyl group in an aromatic compound [30]. The C=O in-plane bending vibration occurs in the range of 820-630 cm^{-1}. El-Azab et al. reported that C=O in-plane bending vibration was appearing at 694 cm^{-1} [31]. For this compound vibration mode was observed as a weak intense peak at 694 (w) cm^{-1} in the FT-IR spectrum. The corresponding in-plane C=O occurs modes in the 695 cm^{-1} for B3LYP/6-31G and 694 cm^{-1} for B3LYP/6-311G. Based on the absorption and emission, the prominent absorptions in the combination of δC = O, δCC, the medium-strong peak is observed in the magnitude of FT-IR is 1094 (ms) cm^{-1}, the corresponding value lies in 1095 cm^{-1} at both B3LYP/6-31G and B3LYP/6-311G.

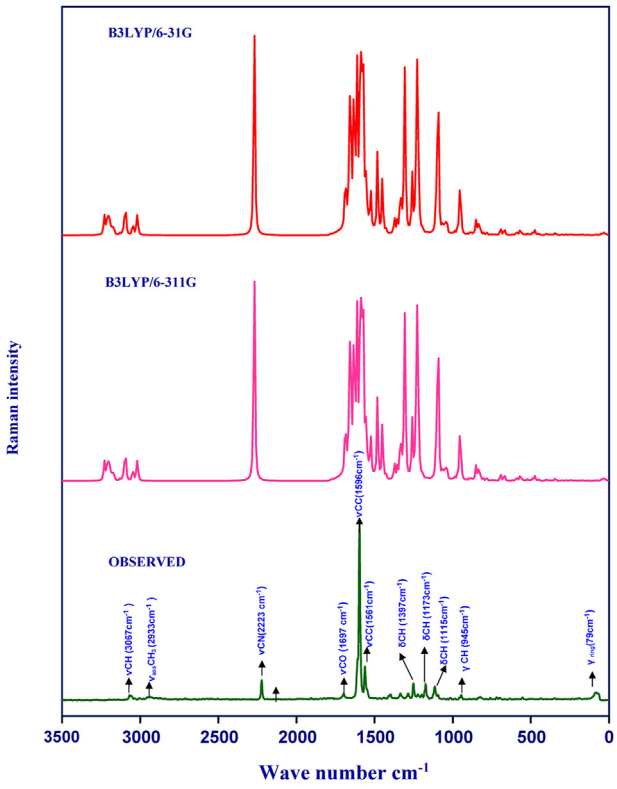

Figure 3. Observed FT-Raman and simulated spectra of CPTBN.

Table 3. Vibrational assignments, observed and calculated wavenumbers (scaled) CPTBN at B3LYP method with 6-31G and 6-311G basis sets.

Mode No.	Observed wavenumbers (cm^{-1})		Calculated wavenumbers (cm^{-1})		Vibrational assignments (PED %)
	FT-IR	FT-RAMAN	B3LYP/6-31G	B3LYP/6-311G	
1		3067m	3075	3067	νCH(98)
2			3060	3061	νCH(98)
3	3049w		3054	3050	νCH(99)
4			3036	3027	νCH(98)
5		3013w	3018	3012	νCH(98)
6			3010	3008	νCH(98)
7			3002	3001	νCH(97)
8			2999	2997	νCH(97)
9			2995	2994	νCH(97)
10			2994	2990	νCH(98)
11			2988	2986	νCH(98)
12			2982	2979	νCH(99)
13			2975	2972	νCH(98)
14	2957w		2966	2960	ν CH(99)
15			2955	2953	ν_{ass} CH_2(88)
16		2947w	2952	2948	ν_{ass} CH_3(89)
17			2928	2924	ν_{ass} CH_3(89)
18		2933w	2936	2932	ν_{ass} CH_3(89)
19	2929w		2934	2930	ν_{ass} CH_3(89)
20			2915	2912	ν_{ass} CH_2(96)
21			2903	2900	ν_{ass} CH_3(96)
22			2881	2879	ν_{ass} CH_3(89)
23	2868w	2868w	2870	2868	νCH(97)
24	2223w	2222ms	2228	2223	νCN(98)
25	1698ms	1697w	1702	1699	νCO(82),δCC(14)
26			1655	1653	νCC(75), δCH(15)
27	1600ms	1596vs	600	1598	νCC(74), δCH(16)
28		1561vs	1564	1562	νCC(74), δCH(15)
29		1551m	1552	1550	νCC(72), δCH(14)
30	1548vs		1550	1548	νCN(72), νCC(12), δCH(10)
31			1525	1522	νCC(88), δCH(16)
32	1493ms	1493w	1498	1495	νCC(78), δCH(10), νCO(10)
33			1455	1453	νCN(72), νCO(14), δCH(10),
34		1441w	1442	1440	νCC(70), νCN(15), νCO(12)
35			1440	1436	δCH(69), νCC(18)
36	1424w		1429	1425	δCH(68), νCC(18)
37			1420	1418	δ_{opb} CH_3(72)
38		1409m	1415	1410	δ_{opb} CH_3(72)
39	1396ms	1397ms	1394	1395	δCH(68), νCCl(20)
40			1390	1389	δ_{ipb} CH_3(82)
41			1385	1382	δ_{ipb} CH_3(82)
42		1375w	1379	1376	ρ_{scis} CH_2(80)
43	1370ms		1370	1368	δCH(69), νCC(10)
44			1345	1343	δCH(68), νCC(12)
45	1331ms	1334ms	1333	1330	δ_{sb} CH_3(69)
46			1325	1322	δCH(62)
47			1314	1312	δCH(66)
48	1306w		1304	1305	δ_{sb} CH_3(72)
49			1300	1296	δCH(67), νCN(10)
50			1293	1290	δCH(69)
51		1285ms	1290	1286	δCH(70)
52			1283	1280	δCH(70)
53	1274ms		1278	1275	δCH(72)
54			1265	1262	γCH(59)
55		1251s	1253	1250	δCH(63)
56			1250	1246	δCH(64)
57			1245	1241	δCH(69)

(*continued on next page*)

Table 3 (*continued*)

Mode No.	Observed wavenumbers (cm^{-1})		Calculated wavenumbers (cm^{-1})		Vibrational assignments (PED %)
	FT-IR	FT-RAMAN	B3LYP/6-31G	B3LYP/6-311G	
58			1240	1237	νCC(70)
59	1225s	1225s	1230	1226	νCC(70), δCC(12)
60			1205	1203	δCH(72)
61	1195ms	1196ms	1196	1194	Γ CH_2(69)
62			1192	1189	δCH(64)
63			1185	1182	δCH(64)
64		1173ms	1178	1175	δCH(64)
65			1154	1151	δCH(63)
66			1140	1137	δCH(63)
67	1114ms	1115ms	1120	1116	δCH(62)
68			1114	1110	νCC(71), δCH(12)
69			1107	1107	Γ CH_2(68)
70		1099ms	1103	1100	δ_{ipr} CH_3(62)
71	1094ms		1095	1095	δCO(66), δCC(22)
72	1058w		1061	1056	δCH(69)
73		1033w	1035	1033	δCH(63)
74			1030	1028	δCH(62)
75			1025	1021	δ_{Opr} CH_3(62)
76	1014w	1012w	1015	1014	νCCL(78)
77			998	998	δ_{ipr} CH_3(70)
78	985w		995	993	νCN(68), νNN(12)
79		980w	980	981	γ CH(66)
80			975	973	δ_{ipr} CH_3(69)
81			966	965	δ_{ring} (58)
82			958	957	δ_{ring} (56)
83	949w		951	949	δ_{ring} (57)
84			948	945	δ_{ring} (60)
85		945m	933	932	γ CH(58)
86			928	925	γ CH(57)
87			920	918	γ CH(58)
88			910	906	γ CH(58)
89	896w		900	898	γ CH(58)
90		889w	893	890	νCH(59)
91			878	875	νCS(78),
92			870	866	νCH(59)
93		850w	853	850	γ CC(68)
94			847	844	γ CC(68)
95		837w	840	838	γ CS(78), νCN(12)
96	829ms		833	829	γ CH(68)
97		823w	826	821	γ CC(68)
98			820	816	γ CH(58)
99	811w		814	810	γ CH(56)
100			793	790	γ CH(58)
101			784	781	γ CH(58),
102			770	767	δ_{ring} (60)
103	748w		753	750	νCH(55)
104			740	738	δ_{ring} (58), νCS(12)
105		720w	724	720	δ_{ring} (60), νCS(12)
106	716w		718	715	δ_{ring} (59)
107		694w	695	694	δ CC(62), δ CO(17)
108	685vw		684	682	γ_{ring} (62)
109		668vw	675	671	γ_{ring} (63)
110	662vw		663	660	γ CO(72)
111			650	647	δ_{ring} (68)
112			641	638	γ CH(58)
113		631m	632	630	δ_{ring} (59)
114	619vw		625	622	γ CC(58), γ_{ring} (20)
115			605	602	δ_{ring} (57), δCN(18)

(*continued on next page*)

Table 3 (*continued*)

Mode No.	Observed wavenumbers (cm^{-1})		Calculated wavenumbers (cm^{-1})		Vibrational assignments (PED %)
	FT-IR	FT-RAMAN	B3LYP/6-31G	B3LYP/6-311G	
116	579w		582	580	δCN(58), δ_{ring} (17)
117			566	564	δCN(58), δ_{ring} (20)
118	554ms	551vw	554	552	δ_{ring} (60)
119			530	528	γ CH(62)
120			520	517	γ CH(60)
121	504w		505	503	γ CH(60)
122	494vw		498	495	γ CH(61)
123			481	479	δ_{ring} (58)
124	460vw		465	462	νCCL(53), δCC(19)
125		440w	444	440	δCC(52)
126			430	427	δ_{ring} (58), δCC(12)
127	406vw		408	405	γ CC(56)
128			400	396	δCC(60)
129			390	388	δCC(60)
130			379	375	γ CC(58)
131			365	363	γ CCH_3(57)
132		353ms	358	355	δ_{ring} (58)
133			345	343	δCC(58)
134			340	339	γ_{ring} (53)
135			334	332	γ_{ring} (54)
136		325w	331	327	γ_{ring} (54)
137			320	319	δCCH_3(56)
138			314	310	γ CC(52), γ_{ring} (21)
139		297w	300	298	γ CC(53)
140			280	275	δCCC(58)
141			255	253	δCCC(60)
142		233w	236	233	γ CCC(52)
143			215	212	δCCC(60)
144			207	202	Γ CH_3(58)
145			190	188	γ CCC(58)
146		181w	185	180	Γ CH_3(58)
147			172	169	γ CCC(53)
148			166	162	Γ CCCC(52)
149			153	151	Γ CCCC(52)
150			148	145	γ CCH_3(62)
151			140	138	δ_{ring} (63)
152		129w	133	130	δCCC(67)
153			128	122	γ CCN(62)
154			125	117	δCCC(63)
155			116	111	γ CCC(60)
156			105	103	δCCC(60)
157		92	97	93	γ CCC(62)
158			95	89	δCCC(60)
159		79s	84	81	γ_{ring} (56)
160			80	76	γ_{ring} (55)
161			75	71	γ_{ring} (55)
162		64s	68	65	γ CCC(54)
163			62	59	γ CCC(54)
164			53	51	γ CCC(50)
165			45	42	γ CCC(52)
166			38	35	γ CC(54)
167			30	29	γ CC(54)
168			25	23	γ_{ring} (52)
169			20	18	γ CC(52)
170			15	14	γ CC(52)
171			10	8	γ CC(51)

s-strong, ms-medium strong, w-weak, vw-very weak, vs-very strong, υ-stretching, ν_{sym}-sym stretching, ν_{ass}-asym stretching, δ-in-plane, δ_{inb}-in-plane bending. δ_{inr}-in-plane rocking, γ-out-of-plane, γ_{opb}-out-of-plane bending, γ_{ring}-out-of-plane ring, scis-scissoring, ρ_{scis}-in plane scissoring, w-wagging, rock-rocking, Γ -twisting, δring -ring vibration.

4.2.7. C–Cl vibrations

The vibrations assignments of the benzene ring belong to C–Halogen (F, Cl, Br) bonds, which are formed between the ring and the halogen atoms are particularly important. Because of the lowering of molecular symmetry and the presence of heavy atoms, vibrations indeed be mixed [32, 33, 34, 35]. In the FT-Raman spectrum, a strong band is observed due to the presence of Cl, Br, and F atoms. Reporting in the FT-Raman spectrum, bands at 720vs cm^{-1} are assigned to C–Cl is stretching vibration observer by Govindarajan et al. [36]. For simple organic chlorine compounds, C–Cl absorptions are in the region between 750–700 cm^{-1}. Sundaraganesan et al. [37] reported C–Cl is stretching at 704 cm^{-1} (IR), 705 cm^{-1} (Raman), and 715 cm^{-1} (DFT) and the deformation bands at 250 cm^{-1} and 160 cm^{-1}. The C–Cl stretching vibration is observed at 460 (vw) cm^{-1} in FT-IR, and the corresponding computed value is 465 cm^{-1} in B3LYP/6-31G and 462 cm^{-1} in 6-311G.

4.2.8. C–S vibrations

The characteristic frequency for the C–S stretching appears as a weak band in the region 800-600 cm^{-1}. In the current study, FT-Raman spectrum with very low intensity is assigned to C–S symmetric stretching vibrations and agreement with the literature value. The C–S stretching modes are reported at 783, 632 cm^{-1} in FT-IR, 633 cm^{-1} in FT-Raman, and 785, 635 cm^{-1} theoretically found by E1-Azab et al. [31]. The C–S stretching vibrations are reported as 770 cm^{-1} in the FT-IR spectrum, and at 770, 636 cm^{-1} theoretically assigned by Fatima et al. [38]. Our FT-Raman shows bands at 720(w) cm^{-1}. The calculated values of C–S stretching vibrations in the thiazole ring are corresponding to 878, 740, 724 cm^{-1} for B3LYP/6-31G and 875, 738, 720 cm^{-1} for B3LYP/6-311G.

4.3. Local reactivity properties of MEP

The molecular electrostatic potential (MEP) plot is a visual illustration of the foremost reactive sites during a molecule and mapped with the rainbow colour scheme (electron made regions represent with red colour, whereas poor lepton regions represent with blue colour and inexperienced shows of zero potential) [39]. Potential will increase within the order red < orange < yellow < green < blue. Using the Gaussian 09 program, we tracked and plotted the alpha density (e-4), density difference (e-3), and MEP (e-2) surface mapping. Surface analysis diagram of title compound net electrostatic effect produced at that point by total charge distribution (electron + proton) of the molecule and correlates with electronegativity, partial charges, and chemical reactivity of the molecules. It provides a visual method to understand the relative step-by-step polarity of the molecule.

Based on the three electrostatic potential surfaces deepest red potential value in this molecule ranges from-4.055e^{-4} a.u, -6.088e^{-3} a.u and -7.960e^{-2} a.u, deepest blue potential value in this molecule ranges from 4.055e^{-4} a.u, 6.088e^{-3} a.u and 7.960e^{-2} a.u. Alpha density represents the full electrophilic region (blue colour). Density difference shows the region energy difference between alpha density and MEP. In the reactive properties of MEP, the nucleophilic reactive site (red colour) shows the molecule's negative regions, and is located on the thiazole ring and partly above the benzonitrile. The other site is the electrophilic reactive site (blue colour) which indicates the positive regions of the molecule and is located on all hydrogen atoms in the molecule. The more dominant green colour over the MEP surface indicates that the electrostatic potential is midway between the vicinity of the red and blue regions. Therefore intermolecular interaction of the compound was confirmed by the reactive site region, the electrostatic potential surface along with the Alpha density, and complete title compound density is shown in Figure 4.

4.4. HOMO-LUMO energy and global reactivity descriptors

The energies of the highest occupied molecular orbital (HOMO), the outermost orbital containing electrons, tend to give electrons and act as an electron donor. On the other hand lowest unoccupied molecular orbital (LUMO), the innermost orbital containing is vacant and can accept electrons. HOMO and LUMO energy gaps between orbits are called frontier molecular orbital (FMOs). In a simple molecule, orbital theory approaches HOMO and LUMO can offer a reasonable qualitative prediction of the excitation properties and the ability of electron transport. The positive surface indicated by red colour and the negative surface is represented by green colour. The energies of the HOMO and LUMO orbital for the possible excitations were carried as 3.57 eV for B3LYP/6-31G and 3.58 eV for B3LYP/6-311G. Based on the root density functional descriptors, global reactivity descriptors of the title molecule described the ionization potential (I), electron affinity (A), chemical potential (μ), electro-negativity (χ), global hardness (η), global softness (σ) and global electrophilicity (ω) value, according to the equations given below [40]. Using HOMO and LUMO orbital energies, the ionization energy (I) and electron affinity (A) can be expressed as Eqs. (1) and (2)

$$\text{Ionization potential } I = -E_{HOMO}\ (E_H) \quad (1)$$

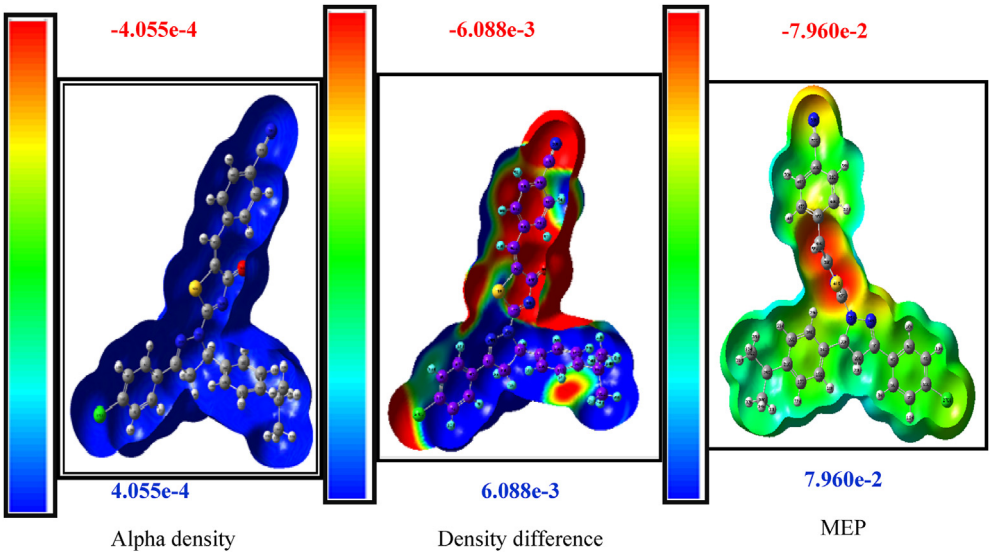

Figure 4. Alpha density (e-4), density difference (e-3), and MEP (Molecular electrostatic potential surface) of CPTBN.

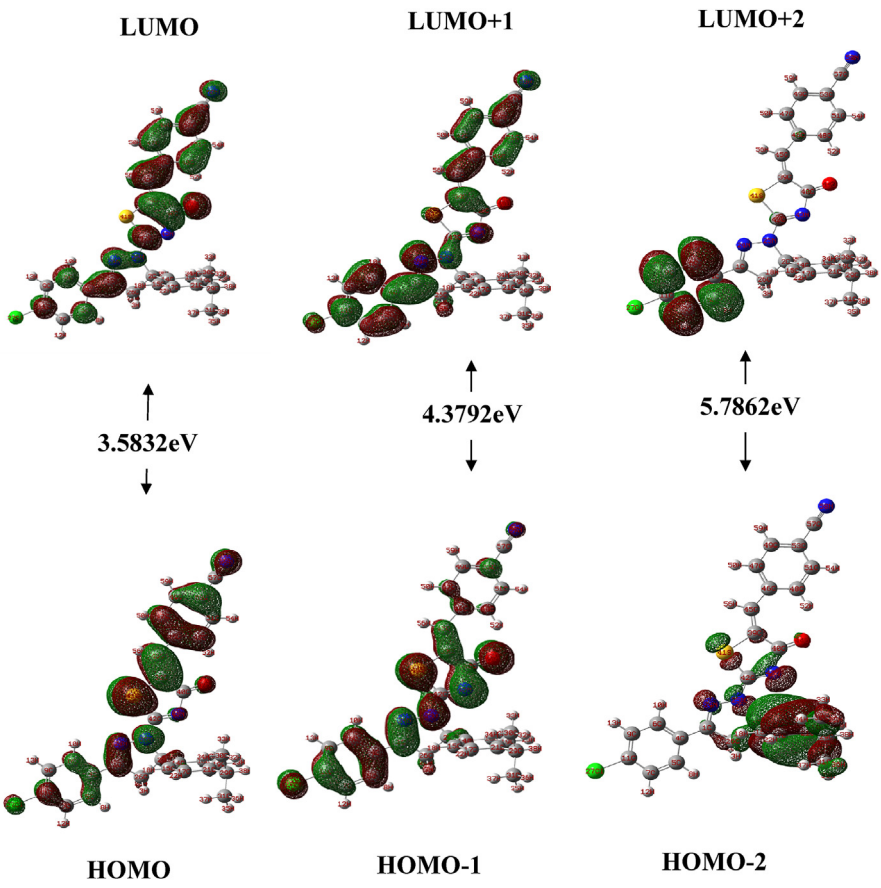

Figure 5. HOMO - LUMO energy distribution plots of CPTBN at DFT/B3LYP/6-311G basis set.

Electron affinity $A = -E_{LUMO}$ (E_L) (2)

Conforming the Koopman's statement that the negative energies of E_{HOMO} were 6.46 eV, 6.70 eV, 6.99 eV and E_{LUMO} were 2.88 eV, 2.32 eV, 1.21 eV. Moreover, the energy gap is calculated with the occurrence of orbital diagram HOMO-LUMO, HOMO-1-LUMO+1, HOMO-2-LUMO+2, and the most significant higher orbital energy gaps were determined in 6-311G at 3.58 eV, 4.37 eV, 5.78 eV (Figure 5). Predict the molecular electronic transitions properties results based on the finding the orbital energy gaps. In a series of E_{HOMO} and E_{LUMO}, it calculates the resistance to change in the electron distribution was defined by

Global hardness $\eta = (I - A)$ (3)

Reactive side of the compound show $\eta = 1.79$ eV, 2.18 eV, 2.89 eV. which was find from the Eq. (3). The global softness Eq. (4) was the inverse of global hardness:

Global softness $\sigma = 1/\eta$ (4)

Value was $\sigma = 0.55$ eV, 0.45 eV, 0.34 eV. Generally, the electron in solids has a chemical potential expressing (negative value of electronegativity - χ) the ability of an uncharged atom or molecule of a chemical system by Eq. (5)

$\mu = - (I + A) /2$ (5)

The power of an atom in a molecule to attract electrons towards it. Value is $\chi = 4.6757$ eV, 4.5107 eV, 4.1059 eV has taken from the Eq. (6)

Electro-negativity is $\chi = (I + A)/2$ (6)

Global electrophilicity, according to Parr et al. [41], evaluates the stabilization energy when the system acquires an additional electronic charge from the environment. The relationship between electrochemical potential and global or chemical hardness can be computed using the following formula (7):

Global electrophilicity index $\omega = \mu\ 2/2\eta$ (7)

The electrophilicity index of the CPTBN, $\omega = 6.1013$ eV, 4.6461 eV, 2.9136 eV. From the result ω, it measures the maximum electron flow

Table 4. Calculated E-HOMO, E-LUMO(H-1→ L+1, H-2→ L+2), energy gap (E_L–E_H), Ionization potential (I), Electron affinity (A), global hardness (η), electronegativity (χ), chemical softness (σ), chemical potential (μ) and global electrophilicity (ω) using the 6-311G levels of theory.

Molecular properties	Energy (eV)	Energy gap (eV)	(I) (eV)	(A) (eV)	(η) (eV)	(χ) (eV)	(σ) (eV)	(μ) (-eV)	(ω) (eV)
E_{HOMO}	-6.4673								
E_{LUMO}	-2.8841	3.5832	6.4673	2.8841	1.7916	4.6757	0.558	-4.6757	6.1013
E_{HOMO-1}	-6.7003								
E_{LUMO+1}	-2.3211	4.3792	6.7003	2.3211	2.1896	4.5107	0.457	-4.5107	4.6461
E_{HOMO-2}	-6.9990								
E_{LUMO+2}	-1.2128	5.7862	6.9990	1.2128	2.8931	4.1059	0.346	-4.1059	2.9136

between donor and acceptor orbits with lower energy transitions. These values of global reactive descriptor are computed and listed in Table 4, which ensures the molecule's indisputable biological activity.

4.5. Fock matrix for bonds

Calculations of the NBO [12] were made using the Gaussian 09 [10] program to interpret the many second-order perturbation interactions between the full orbits of one subsystem and the empty orbits of another subsystem, which is a measure of hyperconjugation intermolecular delocalization. The donor-acceptor interactions in the NBO basis were evaluated using the second-order Fock matrix [42]. The interactions result in a loss of occupancy from the localized NBO of the idealized Lewis structure in an empty non-Lewis orbital. For each donor (i) and acceptor (j), the stabilization energy in the Eq. (8) E (2) associated with the delocalization [i→j] is estimated at

$$E(2) = \Delta Eij = qi\frac{(F_{i,j})^2}{(E_j - E_i)} \quad (8)$$

where q_i is the orbital occupancy of the donor, E_i and E_j are diagonal elements and F (i, j) is the off-diagonal NBO Fock matrix element. The

Table 5. Second-order perturbation theory analysis of Foci matrix in NBO basis corresponding to the intramolecular bonds of the title compounds.

Donor(i)	Type	ED/e	Acceptor (j)	Type	ED/e	E (2)[a] Kcal/mol	E(j)-E(i)[b] a.u	F (i,j)[c] a.u
π	(C_6–C_9)	1.66281	π *	(C_4–C_5)	0.39139	21	0.28	0.069
π	(C_6–C_9)	1.66281	π *	(C_7–C_{11})	0.39379	22	0.26	0.068
σ	(C_6–H_{10})	1.97641	σ *	(C_4–C_5)	0.02245	5	1.06	0.064
π	(C_7–C_{11})	1.67990	π *	(C_4–C_5)	0.39139	18	0.3	0.066
π	(C_7–C_{11})	1.67990	π *	(C_6–C_9)	0.34219	19	0.3	0.069
π	(C_{14}–C_{15})	1.64735	π *	(C_{16}–C_{19})	0.34219	20	0.29	0.067
π	(C_{14}–C_{15})	1.64735	π *	(C_{17}–C_{21})	0.35984	19	0.29	0.067
π	(C_{16}–C_{19})	1.69021	π *	(C_{14}–C_{15})	0.39031	22	0.28	0.07
π	(C_{16}–C_{19})	1.69021	π *	(C_{17}–C_{21})	0.35984	21	0.29	0.071
π	(C_{17}–C_{21})	1.64735	π *	(C_{14}–C_{15})	0.39031	22	0.27	0.069
π	(C17 – C_{21})	1.64735	π *	(C_{16}–C_{19})	0.34219	20	0.28	0.067
σ	(C_{29}–H_{38})	1.84834	π *	(C_{17}–C_{21})	0.35984	12	0.46	0.07
σ	(C_{29}–H_{38})	1.84834	σ *	(C_{30}–H_{34})	0.01601	6	0.86	0.063
σ	(C_{39}–S_{41})	1.97925	σ *	(N_{25}–C_{42})	0.05277	8	1.43	0.096
π	(C_{39}–C_{45})	1.73334	π *	(S_{41}–C_{42})	0.63064	29	0.22	0.079
σ	(C_{40}–N_{43})	1.97841	σ *	(N_{25}–C_{42})	0.05277	6	1.16	0.077
π	(C_{40}–O_{44})	1.91434	LP (2)	N_{43}	1.92042	12	0.17	0.063
π	(C_{40}–O_{44})	1.91434	π *	(C_{39}–C_{45})	0.28300	9	0.27	0.047
π	(S_{41}–C_{42})	1.84834	LP (2)	N_{43}	1.92042	12	0.24	0.072
π	(S_{41}–C_{42}))	1.84834	π *	(C_{39}–C_{45})	0.28300	27	0.34	0.089
π	(C_{46}–C_{48})	1.65062	π *	(C_{47}–C_{49})	0.29371	19	0.29	0.067
π	(C_{46}–C_{48})	1.65062	π *	(C_{51}–C_{53})	0.37039	22	0.28	0.07
π	(C_{47}–C_{49})	1.64135	π *	(C_{46}–C_{48})	0.35121	23	0.28	0.071
π	(C_{47}–C_{49})	1.64135	π *	(C_{51}–C_{53})	0.37039	21	0.27	0.069
π	(C_{51}–C_{53})	1.65616	π *	(C_{46}–C_{48})	0.35121	19	0.29	0.066
π	(C_{51}–C_{53})	1.65616	π *	(C_{47}–C_{49})	0.29371	21	0.29	0.07
LP (1)	N_2	1.99953	σ *	(C_2–N_{25})	0.03916	5	0.81	0.06
LP (1)	N_{25}	1.99913	π *	(C_1–N_{24})	0.01741	26	0.25	0.071
LP (1)	N_{25}	1.99913	σ *	(C_2–H_{55})	0.03916	6	0.61	0.056
LP (1)	N_{25}	1.99913	σ *	(S_{41}–C_{42})	0.04831	7	0.74	0.07
LP (1)	N_{25}	1.74932	σ *	(C_{42}–N_{43})	0.63064	13	0.67	0.087
LP (3)	Cl_{27}	1.92589	π *	(C_7–C_{11})	0.39379	13	0.32	0.062
LP (1)	S_{41}	2.00000	σ *	(C_{39}–C_{40})	0.09788	7	0.95	0.074
LP (1)	S_{41}	1.94182	σ *	(C_{42}–N_{43})	0.05976	7	0.93	0.072
LP (1)	N_{43}	1.99948	σ *	(C_{39}–C_{40})	0.09788	6	0.79	0.064
LP (2)	N_{43}	1.92042	π *	(C_{40}–O_{44})	0.35013	77	0.16	0.112
LP (2)	N_{43}	1.24797	π *	(S_{41}–C_{42})	0.63064	144.68	0.1	0.112
LP (2)	O_{44}	1.97959	σ *	(C_{39}–C_{40})	0.09788	18	0.67	0.099
LP (2)	O_{44}	1.88072	σ *	(C_{40}–N_{43})	0.06721	22	0.65	0.108
LP (1)	N_{58}	1.96668	σ *	(C_{53}–C_{57})	0.03752	11	0.85	0.088
π *	(C_1–N_2)	0.25467	π *	(C_4–C_5)	0.39139	39	0.04	0.064
π *	(C_7–C_{11})	0.39379	π *	(C_4–C_5)	0.39139	215.88	0.02	0.084
π *	(C_7–C_{11})	0.39379	π *	(C_6–C_9)	0.29426	141.93	0.02	0.079
π *	(C_{39}–C_{45})	0.28300	σ *	(C_{40}–O_{44})	0.02004	32	0.06	0.07
π *	(S_{41}–C_{42})	0.63064	σ *	(N_{24} - Ns_{25})	0.03320	5	0.34	0.064

[a] E (2) means energy of hyper conjugative interaction (stabilization energy).
[b] Energy difference between donor and acceptor i and j NBO orbitals.
[c] F (i,j) is the Fock matrix element between i and j NBO orbitals.

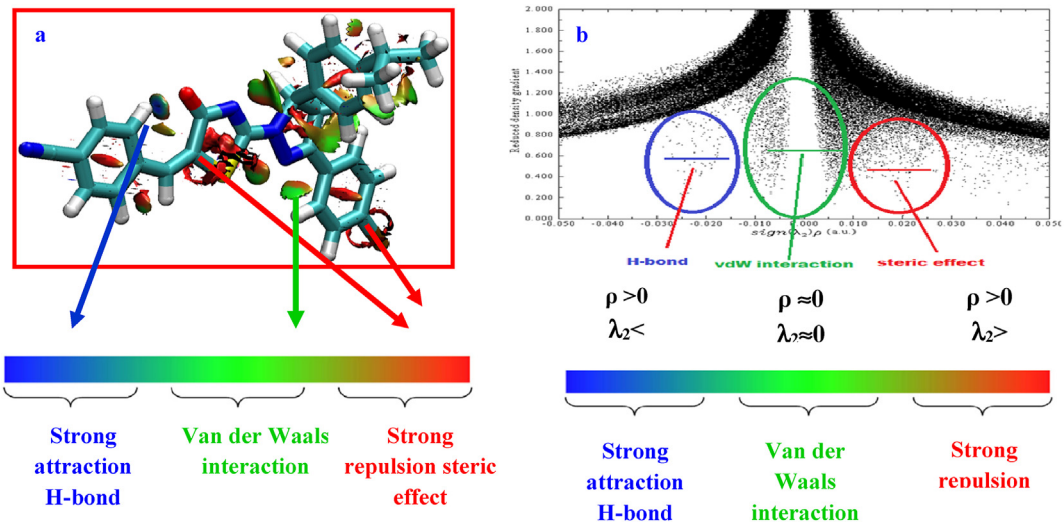

Figure 6. RDG a) 3D colour scaling of non-covalent interaction and b) 2D scatter graph of the electron densityρ versus RDG interaction in CPTBN.

transmission of this electron to electron from a bonding orbital (donor-σ, π) with depreciation in its occupancy [41], an anti-bonding orbital (acceptor - σ*, π*) and Lone pair (LP) can be defined as charge transfer. Several other types of valuable data, such as directionality, hybridization, and partial loading, have been analyzed from the NBO results.

The strong intra-molecular hyperconjugation interaction of the π* electrons from C_7–C_{11} to the π* anti-bonding orbital's of S_{41}–C_{42} bond shows leading to the stabilization of 215.88 kcal/mol. This enhanced π*(C_7–C_{11}) NBO further conjugates with π*(C_4–C_5), π *(C_6– C_9), resulting in enormous stabilization energy of 215.88, 141.93 Kcal/mol, as shown in Table 5. The interaction between π* and π* shows (C_6–C_9), (C_7–C_{11}), and (S_{41}– C_4)$_2$ the electrons is heavy intermolecular. It allows the equilibrium of α kcal/mol, in the (C_6–C_9) to the anti-bonding orbits of (C_{11}–Cl_{27}), (C_4–C_5), and (C_7–C_{11}). In addition to these interactions, there is also a strong lone pair show stabilization capacity, such as LP (1)N_{25} -π *(C_1–N_{24}) 26 kcal/mol, LP (2)N_{43} - π *(S_{41}–C_{42}) 144.68 kcal/mol using 6-311G respectively. These charge transfers are responsible for the structure-activity of the system.

4.6. Reduced density gradient (RDG)

The RDG method is a powerful way to analyze non-covalent intermolecular interactions. The RDG function is a fundamental dimensionless quantity used to describe the deviation from a homogeneous electron distribution, which succeeding Eq. (9) was developed by E. R. Johnson et al. [43].

$$RDG(r) = \frac{1}{2(3\pi r^2)^{1/2}} \frac{|\nabla\rho(r)|}{\rho(r)^{4/3}} \quad (9)$$

where ρ(r) and RDG (r) are the electron density and its first derivative, respectively. The gradient subsurface plots of RDG versus the electron density ρ(r) multiplied by the sign of the second Hessian eigenvalue sign [k2(r)] were rendered by the VMD 1.9.2 program [44] based on outputs of Multiwfn software 4.1 program [45], shown in Figure 6. The RDG surface blue indicates that a stronger interactive hydrogen bond interacts between benzonitrile and thiazole ring, green colour can be identified as van der Waals (VDW) interaction region placed partial half elliptical slab present in the outer part of the title compound and red colour represent the strong repulsion that appears in the centre of the ring system and the strong region or interaction is located in the C–Cl, and thiazole ring atom. The methyl hydrogen-carbon with a hydrogen atom in the ring system as shown in the Figure 6(a).

The density values of the low-gradient spikes (the RDG versus plot) appear to be a good indicator of the strength of the interaction. When 2D is plotting RDG values versus ρit is more meaningful to use the sign of λ_2 is utilized to distinguish the bonded ($\lambda_2 < 0$) from nonbonding ($\lambda_2 > 0$) interactions, plotted in Figure 6(b).

4.7. Localized orbital locator (LOL) and electron localization function (ELF)

The localized orbital locator (LOL) and electron localization function (ELF) is one of the most powerful methods for understanding chemical bonding because it allows the identification of chemically relevant locations in the molecular space where electrons concentrate, such as a bonding, non-bonding and lone pair. This analysis was defined by LOL [γ(r)] and ELF [η(r)] which is related with Fermi hole curvature [46]. And it is defined as a measure of excess Kinetic energy density due to Pauli repulsion. The shaded surface map of electron localization function and localized orbital locator -LOL are drawn using Multi-wfn software [47], they are presented in Figures 7 and 8 respectively. Basins are divided into two categories. On the one hand, core basins are clustered around nuclei (with $Z > 2$), whereas valence basins occupy the remaining area. The inner atomic shell structure is quite similar to the structure provided by the core basins and a valence basin is characterized by a number of the core is connected [48, 49]. In our description, the localization colour code (Figure 7) used for the domain are: red-dot blue ring show the carbon core, red-dot yellow ring show the joining bond between core atoms or inner shell (C–C, C–N) bond and white shell rounded with rings of red, yellow, green show the valence shell (i.e., hydrogen bonding). Next, an electron localization function shows the shaded surface map obtained from localization orbits. Depending upon the density of electron it notify the boundary region are highly localized with board peak (hydrogen regions nearer to 1), the ring bond region is middle localized with a sharp peak (like water droplet) and C≡N region are low localized with small dens peak. shown in Figure 8.

4.8. Antibiotic and antifungal activity

Microbial is killed and ruled out from reproduction by antimicrobial drugs. Nevertheless, these microorganisms are caused by improper and unnecessary use of antibiotics to develop resistance to these substances [3, 50]. Thiazole compound was assayed at a concentration range of 25 μg/ml-violet colour, 50 μg/ml-red colour, 75 μg/ml -green colour, 100 μg/ml-pink colour and total control - blue colour range shown in bar chart Figure 9 against two Gram-positive bacteria: *Bacillus subtilis*, *Staphylococcus aureus* and two Gram-negative bacteria: *Escherichia coli*, *Pseudomonas aeruginosa* Figure 10. The anti-fungal activity was carried

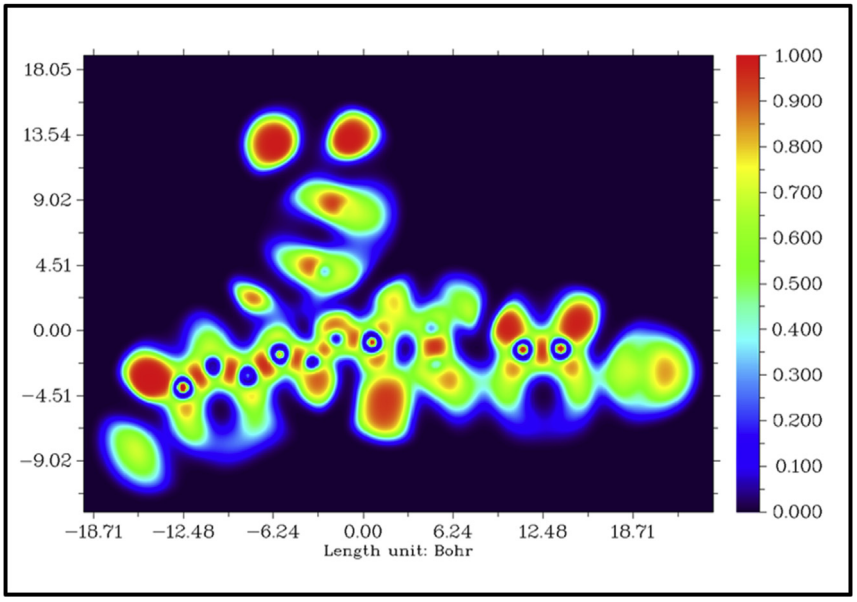

Figure 7. Localized orbital locator (LOL) for CPTBN obtained in xy plane.

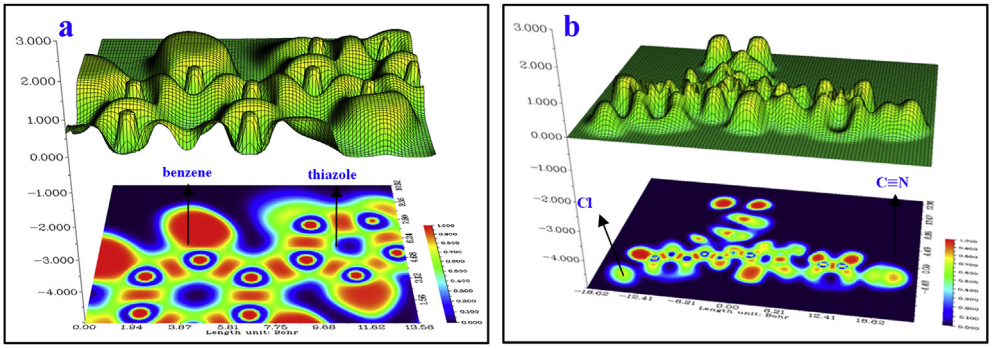

Figure 8. Electron localization function (ELF) or shaded surface map with projection effect of a) thiazole and benzene ring and b) full CPTBN.

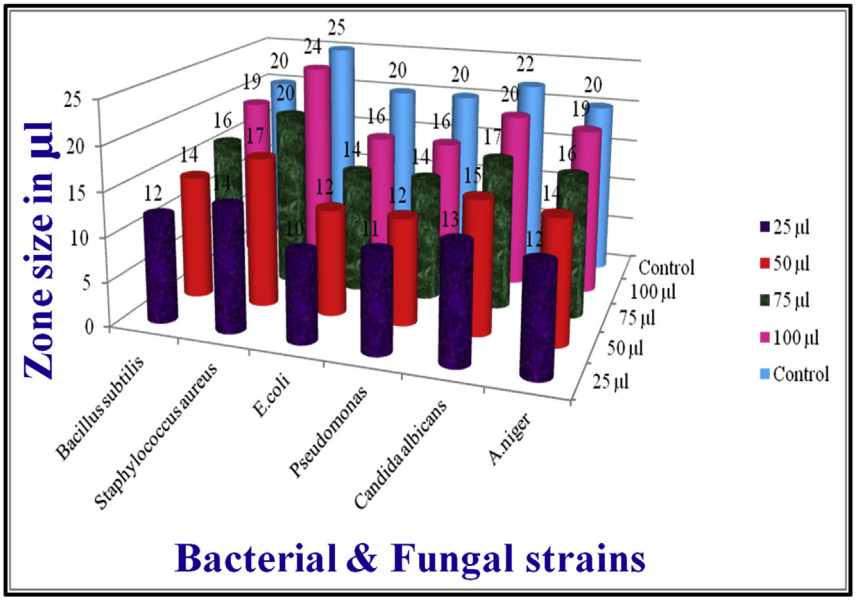

Figure 9. Bar chart for antibacterial and antifungal of CPTBN.

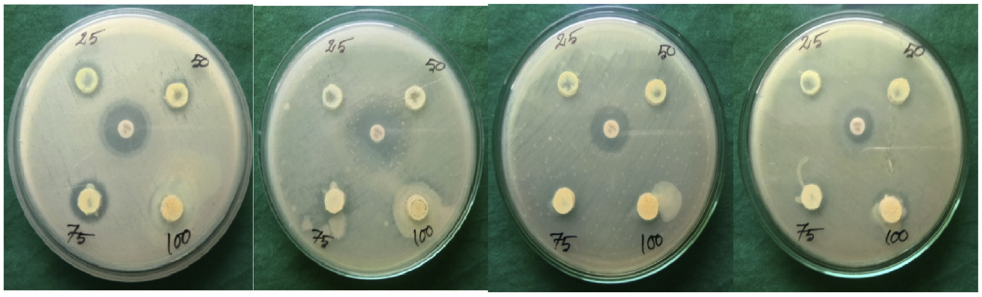

Figure 10. CPTBN microbial tests against bacterial microorganisms a) *Bacillus subtilis*, b) *Staphylococcus aureus*, c) *Escherichia coli* and d) *Pseudomonas aeruginosa* using disk-diffusion method.

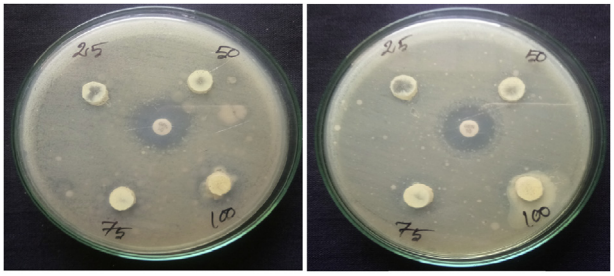

Figure 11. CPTBN microbial testing of fungal microorganism e) *Candida albicans* and f) Aspergillus Niger using Disk-diffusion method.

out against a well-known fungal strain *Candida albicans and Aspergillus Niger* (Figure 11) by the disc diffusion method [51]. Bacterial and fungal pathogens standardized using the DMSO standard were diluted (1:100) and added to an aliquot into respective wells. The plates were incubated in a static incubator at 37 °C for 18–24 h and the determined zone of inhibitory concentration values are listed in Table 6. Results revealed that the compound showed varying zone of inhibition against the test panel of pathogens were plotted in the form of bar graph Figure 9. Notably, the compound showed the highest inhibition against bacterial strains *Staphylococcus aureus*, whereas 24µl respectively at 100 µg/ml. Furthermore, significant inhibition against fungi strains *Candida* Aabicans whereas 20µl showed inhibition at 100 µg/ml against A. Niger is shown in Figures.10 and 11.

4.9. Molecular docking

Molecular docking is a computational technique that tries to predict the sub-region or binding composites from multi-dimensional images of the macromolecule (protein) non-covalent bonding and a small molecule (ligands) [52]. Multiple views of the visualization are a useful way of extending 3D, the 2D display shows dimensional limitations. To collect such views directly from the PDB (protein data bank). Based on the antibiotics, antifungal and biological behaviors of the CPTBN, different types of protein activities such as high-resolution antibacterial, antifungal, Monoclonal antibodies, Nitric oxide synthase inhibitor, Staphylococcal protein A. Taken protein structure has been downloaded from the RCSB [53] PDB ID website of the database 2GOM, 4YDO, 5I76, 4D7O and 1BDC. Initially, the title molecule was minimized as a pdb file based on the DFT method and bind with downloaded protein Finding 3D structures with the lowest binding energy of the compound were constructed using auto dock tools and minimum docking energy values were investigated. The dotted lines show the bond formation between the ligand and targeted proteins. The docking runs were analyzed for the predicted binding interactions, including binding energy, inhibition constant, and intermolecular energy, between the receptors and ligand in the best scoring pose, which was listed in Table 7. Discovery studio [15] generates the binding position of a ligand-protein dock in 3D view (Figures 12a, 12c, 12e, 12g and 12i) and 2D represent (Figures 12b, 12d, 12f, 12h and 12j) represent a residual interaction energy conformation.

4.9.1. Antibacterial activity

Antibacterial activity and virtual screening by molecular docking of staphylococcus aureus is a protein tied to its complementary target to provide bacterial suppression of structure. *Staphylococcus aureus* (PDB ID -2GOM) protein resolution is 1.25 Å having unit cell length a = 59.59Å, b = 59.59Å, c = 45.63Å, and angle α = 90°, β = 90°, γ = 90° [54]. The docking result of CPTBN ligand interaction has shown (Figures 12a and 12b) a binding affinity to the target protein 2GOM, as indicated by the bonding interaction between the ligand and catalytic site amino acids. Glutamine (GLN) from a van der Waals interaction was found near benzonitrile and Lysine (LYS) forms a Pi-Cation interaction near the thiazole ring. Binding energy and inhibition constant are -7.913 kcal/mol and 1.42 µM.

4.9.2. Antifungal activity

Antifungal of a medication used to treat a fungus infection medicine that contains a fungicide. One of the antifungal protein target *Candida*

Table 6. Antibiotic and Antifungal inhibition zone levels of CPTBN.

SAMPLE	DMSO Extract 100 µl added and Zone of inhibition (mm/ml)				
	25 µl	50 µl	75 µl	100 µl	Control
Bacillus subtilis	12	14	16	19	20
Staphylococcus aureus	14	17	20	24	25
E.coli	10	12	14	16	20
Pseudomonas	11	12	14	16	20
Candida albicans	13	15	17	20	22
A.niger	12	14	16	19	20

Table 7. Molecular docking performance results of the compound CPTBN against selective potential protein inhibitors (PDB).

Ligand name	PDB ID	Bond distance (Å)	Amino acid (residues)	Bond	Inhibition Constant (Micromolar-μM/ Nanomolar- nm))	Binding Energy (kcal/mol)	Inter-molecular energy (kcal/mol)
4-[{2-[3-(4-Chlorophenyl)-5-(4-(propan-2-yl)phenyl)-4,5-dihydro-1*H*-pyrazol-1-yl]-4-oxo-1,3-thiazol-5(4*H*)-ylidene}methyl]benzonitrile (CPTBN)	2GOM	3.5	Glutamine (GLN)	van der Waals	1.42 μM	-7.98	-9.47
		3.6	Lysine (LYS)	Pi-Cation			
	4YDO	2.1	Tyrosine (TYR)	van der Waals	16.35nm	-10.62	-12.11
		1.8	Isoleucine (ILE)	van der Waals			
		2.4	Leucine (LEU)	Pi-Alkyl			
		2.9	Tyrosine (TYR)	Pi-Pi T-shaped			
	5I76	2.7	Proline (PRO)	Pi-Alkyl	4.84 μM	-7.25	-8.74
		2.1	Leucine (LEU)	Conventional hydrogen bond			
		2.9	Serine (SER)	van der Waals			
		2.9	Glutamine (GLN)	van der Waals			
	4D7O	1.9	Isoleucine (ILE)	van der Waals	1.63 μM	-7.85	-9.34
		2.4	Glycine (GLY)	van der Waals			
		2.9	Tryptophan (TRP)	Amide-Pi stacked			
		3.3	Phenylalanine (PHE)	van der Waals			
	1BDC	2.1	Phenylalanine (PHE)	Pi-Pi T-shaped	428.64nm	-8.69	-10.18
		2.7	Asparagine (ASN)	van der Waals			
		2.8	Leucine (LEU)	Alkyl			
		2.9	Serine (SER)	Conventional hydroden bond			
		2.8	Glycine (GLY)	van der Waals			

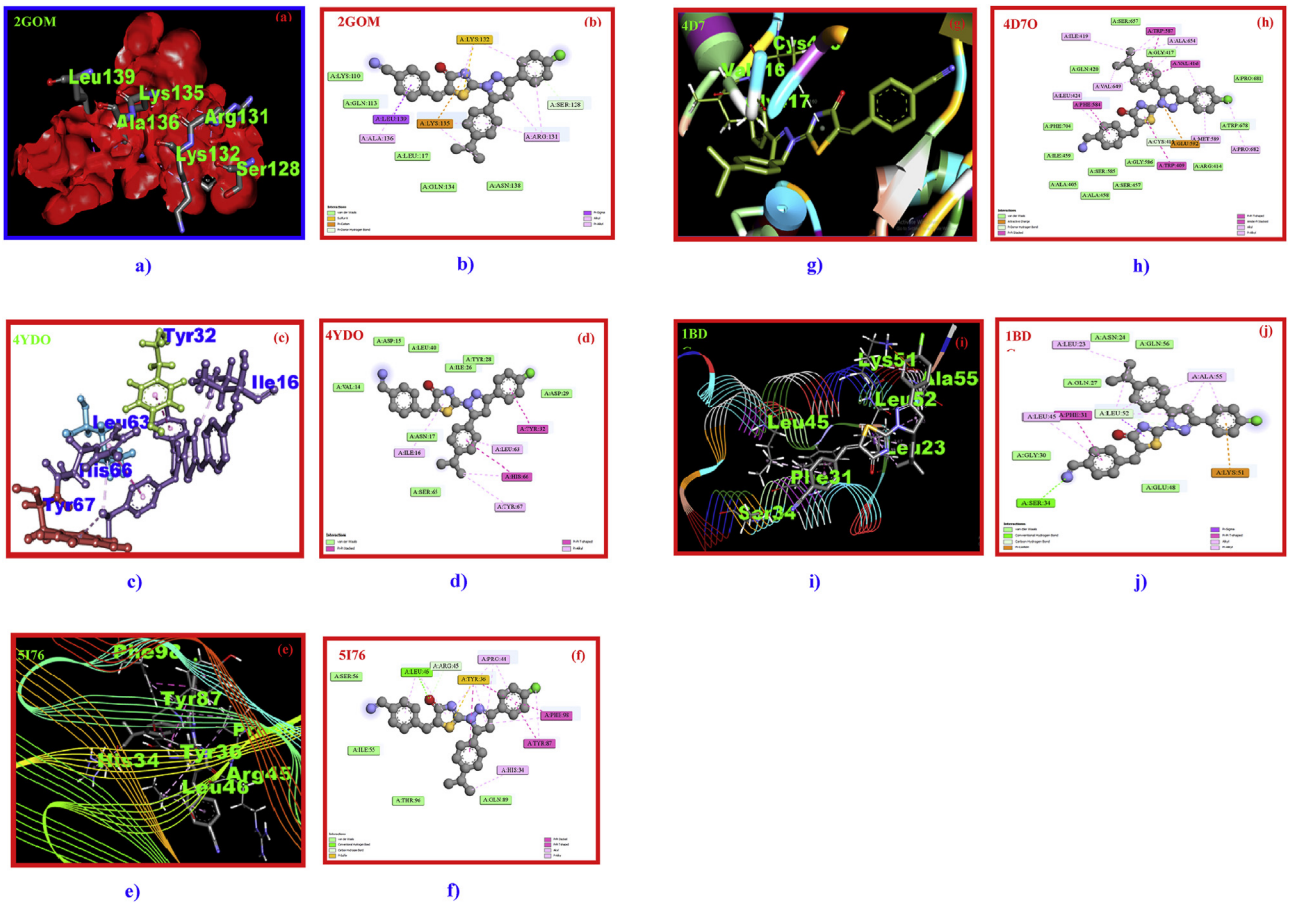

Figure 12. a) Antibacterial Docked interaction pose, b) 2D binding modes of CPTBN structure, c) Antifungal Docked interaction pose, d) residual 2D modes of CPTBN structure, e) Monoclonal antibodies Docked interaction pose, f) targeting 2D modes of CPTBN structure, g) Nitric oxide synthase inhibitor docked interaction pose, h) 2D amino acid bonding modes of CPTBN structure, i) Staphylococcal Protein A docked interaction pose and j) 2D protein interaction modes of CPTBN structure.

Albicans PDB ID: 4YDO are examined ligand (CPTBN) using molecular docking studies. Our aim to verified amino acid (residue) interaction of protein 4YDO are Crystal Structure (Figures 12c and 12d) of *Candida* Albicans Protein Farnesyl transferase in Apo form has a resolution 3.00 Å having a unit cell length a = 96.824 Å, b = 96.824 Å, c = 183.082 Å, and angle α = 90°, β = 90°, γ = 90° [55]. The binding interaction between the ligand and catalytic site amino acids Tyrosine (TYR) and Isoleucine (ILE) forms a Van der Waals interaction near Thiazol ring, Leucine (LEU) forms a Pi-Alkyl interaction and Tyrosine (TYR) forms a Pi-Pi T-shaped interaction. Binding energy and inhibition constant are -10.62 kcal/mol and 16.35 Nanomolar.

4.9.3. Monoclonal antibodies

To develop highly efficient therapeutic and diagnostic agents. Monoclonal antibodies (mAbs) structure of the protein PDB ID: 5I76 is used to simulate the ligand were performed by Auto Dock-Vina Software [56]. 5I76 protein has a resolution 1.922Å having unit cell length a = 72.482 Å, b = 68.037Å, c = 97.689 Å, and angle α = 90°, β = 101.85°, γ = 90°. Examination of the binding energy (-7.85) kcal/mol, inhibition constant (1.76μM) and shown in Figures.12e and 12f. CPTBN ligand bind at the active site of protein by lower amino acid (residue) interaction. Amino acid Leucine (LEU) forms a conventional hydrogen bond with carbonyl present in the thiazole ring. Van der Waals interaction Serine (SER):, Glutamine (GLN): was found near both benzonitrile and propane-2-yl. Proline (PRO) residual alkyl and Pi-alkyl bind with O atom and interaction with the core of the chlorophenyl ring, thiazole ring, and pyrazole ring.

4.9.4. Nitric oxide synthase inhibitor

PDB ID - 4D7O protein (Figure 12g and 12h) [57] has a resolution 1.78 Å had a unit cell length a = 51.77Å, b = 110.58Å, c = 165.16Å and angle α = 90°, β = 90°, γ = 90°.Amino acid Tryptophan (TRP) and Phenylalanine (PHE) forms Amide-Pi stacked and van Der Waals interaction with a CH_3 atom in the propan group. Most of the core rings are interactive with alkyl Pi-Pi, T-Shaped, and amide Pi stacked presented in protein. Two van Der Waals interactions with Isoleucine (ILE) and Glycine (GLY) bound with benzonitrile ring. Binding energy and inhibition constants were -7.85 kcal/mol and 1.63 μM.

4.9.5. Staphylococcal Protein A

Staphylococcal Protein A (PDB ID -1BDC) receptor is a persistent human pathogen that causes a variety of diseases, both in clinical appearance and in severity found in normal human flora, located on the skin and mucous membranes. To investigate nanomolar bacterial binding targets for complementary ligand interaction. Staphylococcal Protein A interaction protein [58] shows (Figures 12i and 12j)the existence of many conventional bonds, which are as follows: Benzonitrile ring form three residual interaction at the same time are Phenylalanine (PHE) form Pi-Pi T-shaped, Serine (SER) form conventional hydrogen bond, Glycine (GLY) form VanderWaals interaction. Leucine (LEU) form carbon-hydrogen bond interaction with the core thiazole ring. Asparagine (ASN) form a van der Waals interaction was found near CH_3. The inhibition constant was 428.64 Nanomolar and the observed binding energy was -8.69 kcal/mol.

5. Conclusion

In the integrating work, analysis of 4-[{2-[3-(4-chlorophenyl)-5-(4-propan-2-yl) phenyl)-4, 5-dihydro- 1H- pyrazol-1-yl]-4-oxo-1, 3-thiazol-5(4H)-ylidene} methyl] benzonitrile [CPTBN] molecule through the first level of the spectral statistics on experimental FT-IR, and FT-Raman are recorded and at the next level, detailed vibrational assignments using DFT/B3LYP/6-31G and B3LYP/6-311G basis level were computed. The geometry of the title molecule is analyzed theoretically. The three different zone mapped surfaces provide a visual plot to understand the atoms in an intermolecular polarity. Positive and negative regions of the MEP map that are localized around the title compound indicate possible sites of nucleophilic and electrophilic reactivity of the molecule. The energy flow from the gap is generally low to high, and Gaussian diagrams have been used to visualize it. The reactive nature of the CPTBN is hypothetically dissected using techniques for the quantum system and addressed by electronic properties, such as hardness, chemical potential, electro-negativity, global hardness, and global softness. The NBO interprets the conjugate relationship of the orbital donor and the unoccupied orbital acceptor in the molecular system. RDG generates the colourful illustration, hydrogen bond, van der Waals and steric effects depict the interaction of the atoms inside the molecule. The electron localization of the region in the molecular space at which identified chemically significant regions as a bond and lone pair. Antimicrobial inhibitory activity against the compound was explored through the tests. Utilizing the molecular restraining nature of the particle was seen as the most vulnerable restricting ligand to a catalyst and the most grounded hydrogen authoritative. The title molecule is docked with receptors high-resolution antibacterial (2GOM), antifungal (4YDO), Monoclonal antibodies (5I76), Nitric oxide synthase inhibitor (4D7O), Staphylococcal protein A (1BDC) and gives good binding affinity values. Acceptable and delicate antibacterial effect against all screened pathogens and the definitive medicine support the docking results. The nature of the molecules shows the binding activity of thiazole with biological targets were examined and discussed in terms of interaction energy. The inclusion of antimicrobial resistance raises to the development of new antibiotics through a direct further rational work mode of action.

Declarations

Author contribution statement

N. Shanmugapriya: Conceived and designed the experiments; Performed the experiments; Analyzed and interpreted the data; Wrote the paper.

V. Balachandran, B. Revathi: Contributed reagents, materials, analysis tools or data.

B. Narayana, Vinutha V. Salian: Performed the experiments.

K. Vanasundari, C. Sivakumar: Analyzed and interpreted the data.

Funding statement

Badiadka Narayana was supported by University Grants Commission (SR/S/Z/-23/2010/32).

Data availability statement

No data was used for the research described in the article.

Declaration of interests statement

The authors declare no conflict of interest.

Additional information

No additional information is available for this paper.

References

[1] B. Gadhiya, M. Rajput, A. Bapodra, K. Ladva, Design, synthesis, and evaluation of antimicrobial activities of some novel thiazole and thiadiazole derivatives clubbed with 1H-Benzimidazole, Rasayan J. Chem. 9 (2016) 355–372.
[2] https://wikimili.com/en/imidazole.
[3] A. Viji, V. Balachandran, S. Babayan, B. Narayana, V.V. Saliyan, FT-IR and FT-Raman investigation, quantum chemical studies, molecular docking study and antimicrobial activity studies on the novel bioactive drug of 1-(2,4-Chlorobenzyl)-3-[2-(3-(4-chlorophenyl)-5-(4-(propan-2-ly)phenyl-4,5-dihydro-1H-pyrazol-1-yl]-4 oxo -4 ,5-dihydro -1,3-thiazol-5(4H)-ylidence]-2,3-dihydro-1H-indol-2-one, J. Mol. Struct. 1215 (2020) 12822244.
[4] E. Nour, A. Abdel-Sattar, A.M. E1-Naggar, M.S.A. Abdel-Mottaleb, Novel thiazole derivatives of medicinal potential: synthesis and modeling, J. Chem (Hindawi) (2017) 1–11.
[5] R.N. Phalen, W.K. Wong, Integrity of disposable nitrile exam gloves exposes to simulated movement, J. Occup. Environ. Hyg. 8 (5) (2011) 289–299.
[6] A.R. Krishnan, H. Saleem, S. Subashchandra bose, N. Sundaraganesan, S. Sebastian, Molecular structure, vibrational spectroscopic (FT-IR, FT-Raman), UV and NBO analysis of 2-chlorobenzonitrile by density functional method, Spectrochim. Acta 78 (2011) 582–589.
[7] A. Ayati, S. Emami, A. Asadipour, A. Shadier, A. Foroumadi, Recent application of 1,3-thiazole core structure in the identification of new lead compounds and drug discovery, Eur. J. Med. Chem. 97 (2015) 699–728.
[8] Vinutha V. Salian, B. Narayana, B.k. Sarojini, M.S. Kumar, A.G. Lobo, Tailor-made heterocyclic pyrazoline- thiazolidinones as effective inhibitors of Escherichia coli FabH: design, synthesis and structural studies, J. Mol. Struct. 1192 (2019) 91–104.
[9] M.J. Frisch, G.W. Trucks, D.J. Fox, Gaussian 09, Revision E.01, Gaussian, Inc., Wallingford CT, 2009.
[10] M.H. Jamroz, Vibrational Energy Distribution Analysis VEDA, 4, Warsaw.S, 2004.
[11] R. Dennington, T. Kerth, J. Millam, Gauss View, Version 5, Semi cham. Inc., Shawnee Mission KS, 2009.
[12] E.D. Glendening, A.E. Reed, J.E. Carpenter, F. Weinhold, NBO Version 3.1, Pittsburg, Theoretical chemistry institute and department of chemistry, University of Wisconsin, Madison, 1988. E.D. Glendening, C.R. Landis, F. Weinhold, Comput. Mol. Sci. 2 (2012) 1.
[13] T. Lu, F. Chen, Multiwfn: a multifunctional wave function analyzer, J. Chem. Inf. Comput. Chem. 33 (2012) 580–592.
[14] G.M. Morris, R. Huey, W. Lindstrom, M.F. Sanner, R.K. Belew, D.S. Goodsell, A.J. Olson, AutoDock4 and AutoDockTools4: automated docking with selective receptor flexibility, J. Comput. Chem. 30 (2009) 2785–2791.
[15] S. Diego, Cailf, Discovery Studio Modeling Environment, Accelry software Release 4.0, USA, 2013.
[16] D. Seeliger, B.L. De Groot, Ligand docking and binding site analysis with Pymol and Auto dock/Vina, J. Comput. Aided Mol. Des. 24 (2010) 417–442.
[17] S. Parveen, M.A. Al-Alshaikh, C. Y Panicker, A.A. El-Emam, Vinutha V. Salian, B. Narayana, Spectroscopic investigations and molecular docking study of (2 E)-1-(4-Chlorophenyl)-3-[4-(propan-2-yl)phenyl]prop-2-en-1-one using quantum chemical calculations, J. Mol. Struct. 1120 (2016) 317–326.
[18] Mustafa Er, Arif Ozer, S. Direkel, T. Karakurt, H. Tahtaci, Novel substituted benzothiazole and Imidazo[2,1-b][1,3,4] thiadiazole derivatives: synthesis, characterization, molecular docking study, and investigation of their in vitro antileishmanial and antibacterial activities, J. Mol. Struct. 1194 (2019) 284–296.
[19] K. Vanasundari, V. Balachandran, M. Kavimani, B. Narayana, Spectroscopic investigation, vibrational assignments, Fukui functions, HOMO-LUMO, MEP and molecular docking evaluation of 4-[(3,4 –dichlorophenyl) amino] 2- methylidene 4 – oxo butanoic acid by DFT method, J. Mol. Struct. 1147 (2017) 136–147.
[20] Priyanka Singh, S.S. Islam, A. Prabaharan, Spectroscopic investigation (FT-IR, FT-Raman), HOMO-LUMO, NBO, and molecular docking analysis of N-ethyl-N-ntrosourea, a potential anticancer agent, J. Mol. Struct. 1154 (2019) 39–50.
[21] M. Sathish, G. Meenakshi, S. Xavier, S. Sebastain, S. Periandy, N.A. Ahmad, J. Jamalis, M.M. Rosli, H. Kun-Fun, Synthiesis, molecular structure, hirshfeld surface, spectral investigation and molecular study of 3-(5-bromo-2-thienyl)-1-(4-fluorophenyl)-3-acetyl-2-pyrazoline(2) by DFT method, J. Mol. Struct. 1164 (2018) 420–437.
[22] S. Beegum, Y. Sheena Mary, C.Y. Panicker, S. Armakovic, S.J. Armakovic, M. Arisoy, O. Temiz-Arpaci, C.V. Alsenoy, Spectroscopic, tantimicrobial and computational study of novel benzoxazole derivative, J. Mol. Struct. 1176 (2019) 881–894.
[23] F.R. Dollish, in: W.G. Fateley, F.F. Bentley (Eds.), Characteristic Raman Frequencies of Organic Compounds, Wiley, New York, 1974.
[24] R.M. Silverstein, G.C. Bassler, T.C. Morrill, Spectrometric Identification of Organic Compounds, John Wiley & Sons, New York, 1981.
[25] S. Fatma, A. Bishnoi, A.K. Verma, Synthesis, spectral analysis (FT-IR, 1 HNMR, 13CNMR and UV-visible) and quantum chemical studies on molecular geometry, NBO, NLO, chemical reactivity and thermodynamic properties of novel 2-amino-4-(4-(dimethylamino)phenyl)-5-oxo-6-phenyl-5, 6-dihydro-4H-pyrano [3, 2-c] quinoline-3-carbonitrile, J. Mol. Struct. 1095 (2015) 112–124.
[26] F. Bardak, Experimental and DFT analysis of structural and spectroscopic features of nitroterephthalic acid, and computational insights into its molecular interactions with hER-a via molecular docking, J. Mol. Struct. 1175 (2019) 458–470.
[27] G.P. Sheeja Mol, D. Aruldas, I.H. joe, S. Balachandran, A.R. Anuf, J. George, Spectroscopic investigation, fungicidal activity and molecular dynamics simulation on benzimidazol-2-yl carbamate derivatives, J. Mol. Struct. 1176 (2019) 226–237.
[28] S.S. Khemalapure, V.S. Katti, C.S. Hiremath, M. Basanagouda, S.M. Hiremath, S.J. Armakovic, Molecular structure, optoelectronic properties, spectroscopic (FT-

IR,FT-Raman and UV-Vis), H-BDE, NBO and drug likeness investigations on 7,8-benzocoumarin-4-acetic acid(7BAA), J. Mol. Struct. 1195 (2019) 815–826.
[29] T.K. Kuruvilla, S. Muthu, J.C. Prasana, J. George, S. Seyyanthi, Spectroscopic(FT-IR, FT-Raman), quantum mechanical and docking studies in methyl[(3s)-3-(naphthalene-1-yloxy)-3-(thiophen-2-yl)propy1]amine, J. Mol. Struct. 1175 (2019) 163–174.
[30] S.C. Jevaseelan, R. Premkumar, K. Kaviyarasu, A. Milton Franklin Benial, Spectroscopic, quantum chemical, molecular docking and in-vitro,anti-cancer activity studies on 5-methoxyindole-3- carboxaldehyde, J. Mol. Struct. 1197 (2019) 134–146.
[31] A.S. E1-Azab, Y. Sheena Mary, C. Yohannan Panicker, Alaa A.M. Abdel-Aziz, Ibrahim A. A1- Suwaidn, C.V. Alsenov, FT-IR, FT-Raman and molecular docking study of ethyl4-(2(4-oxo-3-phenethyl-3,4-dihydroquinazolin-2-ylthio)acetamido) benzoate, J. Mol. Struct. 111 (2016) 9–18.
[32] V. Madhavan, H.T. Varghese, S. Mathew, J. Vinsova, C.Y. Panicker, FT-IR, FTRamanand DFT calculations of 4-chloro-2-(3, 4-dichlorophenylcarbamoyl) phenyl acetate, Spectrochim. Acta 72 (3) (2009) 547–553.
[33] N.P. Roeges, A Guide to the Complete Interpretation of Infrared Spectra of Organic Structures, Wiley, 1994.
[34] E. Mooney, The infra-red spectra of chloro-and bromobenzene derivatives II. Nitro benzenes, Spectrochim. Acta. 20 (6) (1964) 1021–1032.
[35] V. Sortur, J. Yenagi, J. Tonannavar, V.B. Jadhav, M.V. Kulkarni, Spectrochim. Acta A 71 (2008) 688–694.
[36] M. Govindarajan, M. Karabacak, Analysis of vibrational spectra (FT-IR and FT-Raman) and nonlinear optical properties of organic 2-chloro-p-xylene, Spectrochim. Acta 94 (2012) 36–47.
[37] N. Sundaraganesan, S. Ayyappan, H. Umamaheswari, B. Dominic Joshua, FTIR, FTRaman Spectra and ab initio, DFT vibrational analysis of 2,4-dinitrophenylhydrazine, Spectrochim. Acta 66 (2007) 17–27.
[38] S. Fatma, A. Bishnoi, V. Singh, Fatmah A.M. A1-Omary, Ali A.E. Emam, S. Pathak, R. Srivastava, O. Prasad, L. Sinha, Spectroscopic and 1-(2,6-bis (4-methoxyphenyl)-3,3-dimethylpiperidine-4-ylidene)-2-(3-(3, 5-dimethyl-1 H pyrazol-1-yl)pyrazin-2-yl)hydrazine by DFT method, J. Mol. Struct. 1106 (2016) 277–285.
[39] Y.S. Mary, C.Y. Panicker, M. Sapna Kumari, B. Narayana, J.A. War, FT-IR, NBO, HOMO-LUMO, MEP analysis and molecular docking study of 1-[3-(4Fluorophenyl)-5-phenyl-4, 5-dihydro-1H-pyrazol-1-yl] ethanone, Spectrochim. Acta 5 (2015) 483–493.
[40] T.A. Koopmans, Uber die Zuordnung von wellen funktionen and Eigenwerten zu den einzelnen Elektronen Eines Atoms, Physica 1 (1934) 104–113.
[41] R.G. Parr, L.V. Szentpaly, S. Liu, Electrophilicity index, J. Am. Chem. Soc. 121 (9) (1999) 1922–1924.
[42] M. Karabacak, L. Sinha, O. Prasad, Z. Cinar, M. Cinar, The spectroscopic (FT-Raman, FT-IR, UV and NMR), molecular electrostatic potential, polarizability and hyperpolarizability, NBO and HOMO–LUMO analysis of monomeric and dimeric structures of 4-chloro-3,5-dinitrobenzoic acid, Spectrochimica Acta A Mol. Biomol. Spectrosc. 93 (2012) 33–46.
[43] E.R. Johnson, S. Keinan, P. Mori-Sanchez, J. Contreras-Garcia, A.J. Cohen, W. Yang, Revealing non-covalent interactions, J. Am. Chem. Soc. 132 (18) (2010) 6498–6506.
[44] W. Humphrey, A. Dalke, K. Schulten, VMD: visual molecular dynamics, J. Mol. Graph. 14 (1996) 33–38.
[45] T. Lu, F. Chen, A multifunctional wave function analyzer, J. Comput. Chem. 33 (2012) 580–592.
[46] A.D. Becker, K.E. Edgecombe, A simple measure of electron localization in atomic and molecular systems, J. Chem. Phys. 92 (1990) 5397–5403.
[47] S. Noury, F. Colonna, A. Savin, B. Silvi, Analysis of the delocalization in the topological theory of chemical bond, J. Mol. Struct. 450 (1998) 59–68.
[48] K. Jayasheela, Lamya H. Al-Wahaibi, S. Periandy, Hanan M. Hassan, S. Sebastian, S. Xavier, J.C. Daniel, Ali A. El-Emam, M.I. Attia, Probing vibrational activities, electronic properties, molecular docking, and hirshfeld surfaces analysis of 4-chlorophenyl({[(1E)-3-(1Himidazol-1-yl)-1-phenyl propylidene] amino}oxy) methanone: apromising anti-Candida agent, J. Mol. Struct. 1159 (2018) 83–95.
[49] A. Savin, The electron localization function (ELF) and its relatives: interpretations and difficulties, J. Mol. Struct. 727 (1-3) (2005) 127–131.
[50] N. Salih, J. Salimon, E. Youif, Synthesis and antimicrobial activities of 9H-carbazole derivatives, Arab. J. Chem. 9 (2016) 781–786.
[51] E. Yousif, E. Rentschler, N. Salih, J. Salimaon, A. Hameed, M. Katan, Sythesis and antimicrobial screening of tetra schiff bases of 1,2,4,5-tetra (5-amino-1,3,4-thiadiazole-2-yl)benzene, J. Saudi Chem.Soc. 18 (2014) 269–275.
[52] D.B. Kitchen, H. Decornez, J.R. Furr, J. Bajorath, Docking and scoring in virtual screening for drug discovery: methods and applications, Nat. Rev. Drug Discov. 3 (2004) 935–949.
[53] RCSB. http://www.rcsb.org/pdb-structure.
[54] M. Hammel, G. Sfyroera, D. Ricklin, P. Magotti, J.D. Lambris, B.V. Geisbrecht, A structural basis for complement inhibition by staphylococcus aureus, Nat. Immunol. (2007) 430–437.
[55] S. Kumar, M.F. Mabanglo, M.A. Hast, Y. Shi, L.S. Beese, Crystal Structure of Candida Albicans Protein Farnesyltransferase in Apo Form, Wiley, 2013.
[56] O. Trott, A.J. Olson, Software news and update Auto Dock-Vina: improving the speed and accuracy of docking with a new scoring function, efficient optimization, and multithreading, J. Comput. Chem. 31 (2010) 455–461.
[57] T.L. Poulos, H. Li, J.K. Holden, S. Kang, F.C. Beasley, M.A. Cinelli, S.G. Roy, Nitric oxide synthase as a target for Methicillin- resistant Staphylococcus aureus, J. Chem Biol. 22 (2015) 785–792.
[58] H. Gouda, H. Torigoe, A. Saito, M. Sato, Y.J. Arata, I. Shimada, Three-dimensional solution structure of the B domain of staphylococcal protein A: comparisons of the solution and crystal structures, Biochemistry 31 (1992) 199.